

Aerial Cadastral and Flood Assessment for Disaster Risk Management in Appalachia

Daniel Scott Whitehurst

Dissertation submitted to the Faculty of the
Virginia Polytechnic Institute and State University
in partial fulfillment of the requirements for the degree of

Doctor of Philosophy
in
Mechanical Engineering

Kevin Kochersberger, Chair

Mary Kasarda

Venkataramana Sridhar

Danesh Tafti

December 16, 2024

Blacksburg, Virginia

Keywords: Drones, Remote Sensing, Flood Modeling, Emergency Response, Disaster Risk
Management

Copyright 2025, Daniel Scott Whitehurst

Aerial Cadastral and Flood Assessment for Disaster Risk Management in Appalachia

Daniel Scott Whitehurst

(ABSTRACT)

As natural disasters have continued to become more prevalent in recent years, the need for effective disaster management efforts has become even more critical. Flooding is an extremely common natural disaster which can cause significant damage to homes and other property. Using low-cost drones, 3D cadastre models can be created and combined with flood models to quantify individual building risk before, during, and after flood events. As severe flooding devastated areas nearby to Virginia Tech, the need for accurate flood risk quantification became evident. In this work, we focused on the Appalachian area of the United States for flood modeling. The unique terrain of this area coupled with increasing major weather events has led to devastating flooding in the area. In particular, we focused on an area in Southwest Virginia, Hurley, due to a devastating flood event in 2021 as well as its proximity to Virginia Tech. Digital Elevation Models from before the flood and available weather data are used to perform simulations of the flood event using HEC-RAS software. These were validated with measured water height values and found to be very accurate, with errors as low as 2 percent. After this, simulations are performed using the Digital Elevation Models created from drone imagery collected after the flood, and we found that a similar rainfall event on the new terrain would cause even worse flooding, with water depths between 29% and 105% higher. Simulations like these could be used to guide recovery efforts as well as aid response efforts for any future events. After this, a major flood event in 2022 shifted our focus to an area in Eastern Kentucky. The terrain in this area has been affected by

significant surface coal mining, which became a focus due to the limited amount of research into the impacts of surface coal mining on flooding. Through the digitization of historical topographic maps, pre-mining terrain and land cover is compared to the current landscape with respect to runoff and flood potential. Additionally, multiple mine reclamation methods, including the regrowth of forest, grassland, or shrubland, were looked at to reduce the risk of major flooding in the future after mining has been completed. SWAT simulations showed a significant increase, as large as high as 55.8 percent, in surface runoff from the coal mining in the area. HEC-RAS simulations showed localized increases in flooding resulting from mine lands, with some areas seeing an increase of over 2 feet of water depth. Mine reclamation methods show the potential to reduce the amount of surface runoff, by as much 1 foot of water depth, although these ideal scenarios still do not reach pre-mined levels. While the impact which surface mining has had on the environment can not be fully reversed, significant improvements can be made to prevent future flooding in these areas. After these flood case studies, the water depth modeling is combined with high-resolution cadastre data to produce accurate flood risk assessments for the community and property level.

Aerial Cadastral and Flood Assessment for Disaster Risk Management in Appalachia

Daniel Scott Whitehurst

(GENERAL AUDIENCE ABSTRACT)

As natural disasters have continued to become more prevalent in recent years, the need for effective disaster management efforts has become even more critical. Flooding is an extremely common natural disaster which can cause significant damage to homes and other property. Using aerial imagery, 3D models of buildings and property can be created and combined with flood models to quantify flood risk. As severe flooding devastated areas nearby to Virginia Tech, the need for accurate flood risk quantification became evident. In this work, we focused on the Appalachian area of the United States for flood modeling. The unique terrain of this area coupled with increasing major weather events has led to devastating flooding in the area. In particular, we focused on an area in Southwest Virginia, Hurley, due to a devastating flood event in 2021 as well as its proximity to Virginia Tech. The terrain from before the flood and available weather data are used to simulate the flood event using a software program known as HEC-RAS. After this, flood event simulations are performed using the updated terrain models created from aerial imagery collected after the flood. These flood depth simulations showed that a similar rainfall event on the new terrain would cause even worse flooding, with water depth doubling in one area. This information could be used to guide recovery efforts as well as aid response efforts for any future events. After this, a major flood event in 2022 shifted our focus to an area in Eastern Kentucky. This area has been affected by significant surface coal mining, which became a focus to determine the impact of mining on floods. Pre-mining terrain and land cover is compared

to the current landscape with respect to flooding. Additionally, multiple mine reclamation methods, including the growth of forests, grasslands, or shrubs, were looked at to reduce the risk of major flooding in the future after mining has been completed. Hydrological simulations showed a significant increase in water runoff, as large as 55.8 percent, from the coal mining in the area. Flood depth simulations showed localized increases in flooding resulting from mine lands, with some areas increasing by over 2 feet of water depth. Mine reclamation methods show the potential to reduce the amount of surface runoff, although not quite to pre-mined levels. While the impact which surface mining has had on the environment can not be fully reversed, significant improvements can be made to reduce future flooding in these areas. After these flood case studies, the water depth modeling is combined with high-resolution property data to produce accurate flood risk assessments for the community and property level.

Contents

List of Figures	x
List of Tables	xvi
1 Introduction	1
1.0.1 Novel Contributions	1
1.0.2 Software Overview	3
2 Drone-Based Community Assessment, Planning, and Disaster Risk Management for Sustainable Development	6
2.1 Abstract	6
2.2 Introduction and Motivation	7
2.3 Drone-Based Data Collection and Analysis	9
2.3.1 Motivational Forces in Disaster Risk Management	9
2.3.2 Down-Sized and Low-Cost Drone Technology	10
2.3.3 Machine Learning with Drone Imagery	13
2.4 Data Collection and Registration	14
2.4.1 Cadastre Systems and Data	14
2.4.2 Natural Disaster Risk Applications and Data	15

2.4.3	3D Modeling	16
2.4.4	3D Building Size Estimation	18
2.4.5	Contextualizing 3D Models with Cadastre and Risk Data	25
2.5	Discussion and Conclusions	27
3	Post-Flood Analysis for Damage and Restoration Assessment Using Drone Imagery	29
3.1	Abstract	29
3.2	Introduction	30
3.3	Materials and Methods	32
3.3.1	Test Area	32
3.3.2	Test Area Data Collection	33
3.3.3	Image Reconstruction Software	37
3.3.4	Flood Analysis Software	37
3.3.5	Workflow	38
3.4	Drone Image Reconstruction	39
3.4.1	OpenDroneMap Reconstructions	39
3.4.2	Comparison and Interpretation of Visual Data	40
3.5	Flood Simulations	42
3.5.1	HEC-RAS Flood Event Simulation	42
3.5.2	Flood Water Depth Accuracy	45

3.5.3	HEC-RAS Simulation on Post-Flood Environment	48
3.6	Damage Analysis Using Semantic Segmentation	50
3.6.1	Dataset Description and Training	51
3.6.2	Segmentation Results	52
3.7	Conclusions	54
4	The Impact of Surface Mining and Mine Reclamation on Surface Runoff and Flood Risk in Appalachia	57
4.1	Abstract	57
4.2	Introduction	58
4.3	Materials and Methods	61
4.3.1	Investigation Area	61
4.3.2	Pre-Mined and Post-Mined Terrain	62
4.3.3	Simulation Input Data	65
4.4	Surface Runoff Simulations	67
4.4.1	Simulation Parameters	68
4.4.2	Simulation Results	71
4.5	Flood Depth Simulations	72
4.5.1	Simulation Inputs and Parameters	73
4.5.2	Simulation Results	78
4.6	Discussion and Conclusions	81

5 Combining Flood Risk and Property Value to Estimate Loss and Damage	
Risk	83
6 Summary and Conclusions	86
Bibliography	89

List of Figures

2.1	The location of a school in Afghanistan before and after a flood (Satellite imagery: ESRI). This flood of the Amu Darya river occurred in April 2018. .	9
2.2	A school constructed in an Amu Darya river flood plain in Afghanistan and partially destroyed by flooding. This image was provided by Development Monitors LLC.	10
2.3	A comparison of the three smallest drones produced by DJI. This comparison tool is available on the DJI website [59].	11
2.4	Our small, low-cost drone which weighs under 250 grams.	12
2.5	Sample cadastre system used in Montgomery County, VA, USA [2].	14
2.6	Property boundary data displayed in QGIS for the Virginia Tech Kentland research farm.	15
2.7	3D landslide risk map of two communities in Badakhshan province, Afghanistan. This image was provided by Development Monitors LLC.	16
2.8	A 3D reconstruction produced from drone imagery captured at the Virginia Tech Kentland research farm.	18
2.9	BUilding segmentation results for a drone image captured of the Dzaleka refugee camp in Malawi.	19
2.10	Segmentation results for an example test image of a rural area of Afghanistan.	20

2.11	Segmentation results on a test image before and after retraining. The top left shows the original image with the ground truth labels on the bottom left. The top right image shows the detected buildings with the original model. The bottom right image shows the detected buildings with the updated models.	21
2.12	Two examples of building facade segmentation results.	23
2.13	An example of the building facade segmentation and outline. The detected facade polygon is compared to the actual facade polygon in the right image.	23
2.14	A second building facade detection example. The detected outline is overlaid on the original image in the image on the right.	24
2.15	A 3D reconstruction orthophoto produced from drone imagery captured at Kentland Farm overlaid on satellite imagery and cadastre data in QGIS.	27
3.1	A map with a pin marking the location of Hurley, VA is shown on the left. The right portion shows a DJI Mavic Air 2 drone [32], which was used to capture imagery at the test area in Hurley.	34
3.2	Digital Elevation Model of a small section of Guesses Fork Road in Hurley, Virginia.	35
3.3	Example Multi-sensor Quantitative precipitation estimation data for the Guesses Fork Road area of Hurley, Virginia. The data is being displayed in the Operational Product Viewer [35].	36
3.4	3D reconstruction of a portion of Guesses Fork Road in Hurley, Virginia.	39
3.5	3D reconstruction of a portion of Guesses Fork Road in Hurley, Virginia.	40

3.6	A comparison of pre-flood satellite imagery to post-flood imagery. The image on the left shows Google Maps satellite imagery. The image on the right shows the post-flood orthophoto overlaid on the satellite image in GIS (Geographic Information System) software.	41
3.7	A comparison of pre-flood satellite imagery to post-flood imagery. The image on the left shows Google Maps satellite imagery. The image on the right shows the post-flood orthophoto overlaid on the satellite image in GIS software.	41
3.8	Multi-sensor Quantitative precipitation estimation data for one portion of Guesses Fork Road.	44
3.9	HEC-RAS simulated water depth values using the Digital Elevation Models from the Virginia Lidar dataset. This represents the terrain before the flooding event occurred.	45
3.10	The first flood depth measurement location marked on an orthophoto overlaid on satellite imagery. This measurement was taken at one of the houses along Guesses Fork Road.	46
3.11	The second and third flood depth measurement location marked on an orthophoto overlaid on satellite imagery. The second measurement was taken along the stream, next to the road. The third measurement was taken at the railroad bridge at the end of the road.	47
3.12	HEC-RAS simulated water depth values using a post-flood environment Digital Elevation Model. This is the same area as the simulation in Figure 3.9.	49
3.13	Distribution of pixels for each class in the Hurley dataset	52
3.14	Original Image and Ground Truth	53

3.15	Semantic segmentation results comparison of DeepLabV3+, PSPNet and UNet	54
4.1	A representation of surface coal mining from the EPA. The former mountain contour is removed in order to reach the coal seam, while the excess rocks are disposed of by filling adjacent valleys [43].	59
4.2	An aerial image of the flash flooding in Eastern Kentucky during the July 2022 event. The flood waters can be seen covering many streets and partial houses. From Leandro Lozada/AFP via Getty Images, published on npr.org [70].	60
4.3	A screenshot of the investigation area taken from QGIS with Google Maps base imagery. The cities of Hazard and Jackson are labeled along with the mined land area of interest for this work.	62
4.4	The composite DEM created from the data available in the KyFromAbove dataset. The color scale on the right shows the terrain height between 675 and 1908 feet.	63
4.5	Topographic map comparison for one of the mined areas. The map on the left shows the terrain contours from 1972, before significant mountaintop removal occurred. The map on the right shows the terrain in 2022, after the removal of many mountaintops.	64
4.6	The digitization of the topographic map contours performed in QGIS. The left image shows the contours from the topographic map document. The image on the right shows shapefiles created in QGIS based upon these contours. . .	64

4.7	A comparison of the terrain in a mined area. The image on the left shows the present terrain downloaded from the Kentucky database. The image on the right shows a recreation of the terrain from 1972. The mountaintops and valleys can be distinctly seen compared to the present terrain.	65
4.8	The location of the USGS monitoring stations in Hazard, Kentucky and Jackson, Kentucky. This was taken as a screenshot of the image provided by USGS [103].	66
4.9	The precipitation from the NOAA MRMS system measured over a 72 hour period for the investigation area between Hazard and Jackson. Peak areas received over 12 inches of rainfall during this 72 hour window.	66
4.10	The study area used for the SWAT simulations. The North Fork of the Kentucky River and connected streams are shown by the blue lines in the image. The mined areas can be seen nearby portions of the river.	67
4.11	The land cover of the area acquired from the 2021 NLCD. The ID on the right shows the colors corresponding to the land cover types.	68
4.12	The soil types of the area acquired from the SSURGO Database. The ID on the right shows the colors corresponding to the soil types.	69
4.13	The watershed delineation in SWAT. The blue lines represent the stream reaches and the red outlines represent the subbasins.	71
4.14	The streamflow discharge measured at the monitoring station in Hazard, Kentucky between July 25 and July 31 2022.	74

4.15	The location of three measurements used for comparison for the HEC-RAS simulation results. The locations represent the stream nearby, between, and just downstream of the mined areas of interest.	77
4.16	The full investigation area showing the three locations from Figure 4.15 along with the locations of the monitoring stations in Hazard and Jackson.	78
4.17	A comparison of the HEC-RAS water depth results over time for three of the simulations. These include the current mine land with barren land cover, the pre-mined terrain with forest land cover, and the reclaimed scenario with forest land cover.	80
4.18	A comparison of the HEC-RAS water depth results from two the simulations. The left image shows results for an area of mined terrain with barren land cover. The image on the right shows the corresponding area of pre-mine terrain with deciduous forest land cover.	81
5.1	An orthophoto created from the drone imagery captured at Hurley, Virginia.	83
5.2	Detected building polygons were overlaid onto the orthophoto in Hurley. . .	84
5.3	Flood water depths displayed in QGIS with the orthophoto and detected buildings for a section of Hurley, Virginia.	85

List of Tables

2.1	Accuracy results for the building segmentation performed on a test set of images from Afghanistan.	20
2.2	Accuracy results for the building segmentation performed on a test set of images from Afghanistan before and after training.	22
2.3	Accuracy results for the building facade detection and size estimation.	25
3.1	General workflow for our flood response and recovery tools.	38
3.2	A comparison of the water depth from the HEC-RAS simulation and the measured values during our visit to Hurley.	48
3.3	A comparison of the water depth from the HEC-RAS simulation using pre-flood and post-flood terrain.	50
3.4	Mean IOU results for each class on the Test Set	54
4.1	The average surface runoff per year resulting from the SWAT simulations for each of the six terrain and land cover combinations.	72
4.2	The Manning’s N and Percent Impervious values used for each of the land cover types in the HEC-RAS simulations. The NLCD ID numbers and class names are included for each.	75
4.3	The flood depths at four different locations for each of the six HEC-RAS simulations.	79

List of Abbreviations

CNN Convolutional Neural Network

CREST Coupled Routing and Excess Storage

DEM Digital Elevation Model

DRM Disaster Risk Management

DSM Digital Surface Model

DTM Digital Terrain Model

EPA Environmental Protection Agency

FEMA Federal Emergency Management Agency

GIS Geographic Information System

HEC-RAS Hydrologic Engineering Center's River Analysis System

HRU Hydrologic Response Unit

IoU Intersection over Union

LiDAR Light Detection and Ranging

MRMS Multi-Radar/Multi-Sensor System

NLCD National Land Cover Database

NOAA National Oceanic and Atmospheric Administration

ODM OpenDroneMap

QPE Quantitative Precipitation Estimate

SWAT Soil and Water Assessment Tool

UAV Unmanned Aerial Vehicle

USGS United States Geological Survey

Chapter 1

Introduction

The idea for this work began from an international standpoint for low-resource areas, including parts of Africa and Afghanistan. In these areas, accurate cadastral data is very limited or nonexistent. A cadastre is a comprehensive recording of the real estate or properties and their boundaries for a country. This is often represented graphically in a cadastral map. While this data is more available in the United States, this data is not always kept up-to-date. As a result of this, we found a major need for high-resolution, accurate, and up-to-date cadastral data which could be produced from aerial imagery captured from drones. The combination of this cadastral data with flood modeling can produce highly accurate flood risk maps at the property level, which are not currently available. As more flood events began occurring nearby the Virginia Tech campus, in Southwest Virginia and Eastern Kentucky, the focus shifted towards the Appalachian area of the United States due to its unique landscape and proximity. While the focus location shifted, the overall concept of this work is still applicable in the original low-resource international communities as well as many other areas of the world.

1.0.1 Novel Contributions

The Federal Emergency Management Agency (FEMA) in the United States has a nationally standardized risk assessment tool known as Hazus [62]. This offers tools and methodologies

for estimating risk and potential losses from natural disasters including floods, hurricanes, earthquakes, and tsunamis [63]. While this can be extremely useful, large-scale assessment tools use datasets with low geospatial accuracy resulting in less accurate risk estimates. A study in Iowa looked at quantifying flood risk assessment at the community and property level. This found that existing risk products based on FEMA's flood risk output underestimate the flood loss [111].

While flood modeling has been more commonly used to examine the risk and potential impact of flood events in many areas, there is a major lack of modeling the impact and risk of flooding after a flood event has already impacted and damaged a community. In addition to this, the currently available flood risk assessment tools use low resolution and out-of-date terrain data compared to what can be acquired by drones. This work aims to fill the gaps in what is currently available to provide all communities, especially low-resource ones, with a complete flood risk, response, and restoration tool. The flood modeling in this work focuses on the Appalachian area of the United States, specifically areas in Southwest Virginia and Eastern Kentucky which experienced major flooding. The flood modeling in Virginia provides insight on the risk after a flood event has occurred which will enable restoration efforts to help protect the community. In Kentucky, the impact of mined lands and reclamation efforts is quantified. While some previous articles have looked at the impact of these mined areas, studies to quantify this impact have been lacking. This work aims to fill missing gaps and provide useful information about methods of reducing flood risk due to these mines in the future.

This dissertation is divided into three main chapters, with each coming from a separate journal publication. The first chapter contains my portion of the journal article titled "Drone-Based Community Assessment, Planning, and Disaster Risk Management for Sustainable Development"[106] which looks at aerial data collection, 3D cadastre modeling, and

disaster risk assessment using low-cost drones. The second chapter is comprised of the journal article title "Post-Flood Analysis for Damage and Restoration Assessment Using Drone Imagery"[107] which looks at the impacts of a flood event in Hurley, Virginia in 2021. The final chapter is an article which is in the submission process titled "The Impact of Surface Mining and Mine Reclamation on Surface Runoff and Flood Risk in Appalachia". This work examines a flood event in eastern Kentucky in 2022 and the impact of surface coal mining to runoff and flooding in the area. The final chapter will then summarize and tie the three articles together.

1.0.2 Software Overview

Three main software packages have been used throughout the work in this dissertation. OpenDroneMap is used for producing maps and 3D models from aerial imagery. SWAT is used for watershed and surface runoff modeling. HEC-RAS is used for hydraulic floodplain modeling. These programs will be explained in more detail in this section.

OpenDroneMap

OpenDroneMap is an open source toolkit for processing aerial imagery to produce two and three dimensional geographic data. The output data includes orthorectified imagery, digital elevation models, textured 3D models, and classified point clouds [22]. A set of aerial images with significant image overlap is required to produce accurate 3D models. OpenDroneMap uses Structure From Motion in order to build 3D models from the images. For this, OpenDroneMap uses the OpenSfM library [19] to reconstruct camera poses and produce 3D scenes from multiple images. The OpenMVS (Multi-View Stereo) library [45] is used to generate a dense point cloud and mesh surface of the scene. After this, the Geospatial Data Abstrac-

tion Library (GDAL) [65] and the Point Data Abstraction Library (PDAL) [54] are used for georeferencing and generating orthomosaics [49].

SWAT

SWAT (Soil and Water Assessment Tool) is a river basin scale model which can be used to quantify the impact of land management practices in large, complex watershed. SWAT is a public domain hydrology model which includes weather, surface runoff, return flow, percolation, evapotranspiration, transmission losses, pond and reservoir storage, crop growth and irrigation, groundwater flow, reach routing, nutrient and pesticide loading, and water transfer [64]. SWAT is a continuous time model which uses a daily time step at the basin scale. This can be used to simulate water and nutrients cycles and help in assessing the environmental efficiency of best management practices and policies [8]. SWAT performs a preliminary subbasin identification based on topographic criteria then further discretizes this using land use and soil type considerations. Areas with the same topographic characteristics, soil type, and land use form a Hydrologic Response Unit (HRU). An HRU is a basic computational unit which is assumed to be homogeneous in the hydrologic response to land cover change [8]. In this work, SWAT is used in order to simulate the surface runoff changes due to surface coal mining in Eastern Kentucky.

HEC-RAS

HEC-RAS (Hydrologic Engineering Center's River Analysis System) is an open source software created by the US Army Corps of Engineers which is designed to perform one and two-dimensional hydraulic calculations for a full network of natural and constructed channels. This software is used to model the hydraulics of water flow through natural rivers

and other channels [1]. The HEC-RAS system has the ability to perform steady flow water surface profile computations, one- and two-dimensional unsteady flow simulations, movable boundary sediment transport computations, and water quality analysis [1]. For steady flow, HEC-RAS performs the computations based on the solution of the one-dimensional energy equation. For unsteady flow simulations, HEC-RAS uses an implicit, finite difference method in order to solve the dynamic 1-D Saint Venant Equation. Due to the finite difference numerical solution methods for unsteady flow analysis, numerical instability problems can occur, especially in steep or highly dynamic rivers and streams [6]. These numerical stability issues can be overcome through adjustments to the simulation time step and mesh size along with parameters for the simulation Courant number. In this work, HEC-RAS is used to simulate flood depths in an area of Southwest Virginia as well as Eastern Kentucky.

Chapter 2

Drone-Based Community Assessment, Planning, and Disaster Risk Management for Sustainable Development

The majority of this chapter was previously published in the journal *Remote Sensing* with the title "Drone-Based Community Assessment, Planning, and Disaster Risk Management for Sustainable Development" [106]. Only the portions of the paper with my work are included in this chapter.

2.1 Abstract

Accessible, low-cost technologies and tools are needed in the developing world to support community planning, disaster risk assessment, and land tenure. Enterprise-scale geographic information system (GIS) software and high-resolution aerial or satellite imagery are tools which are typically not available to or affordable for resource-limited communities. In this paper, we present a concept of aerial data collection, 3D cadastre modeling, and disaster risk assessment using low-cost drones and adapted open-source software. Computer vision/ma-

chine learning methods are used to create a classified 3D cadastre that contextualizes and quantifies potential natural disaster risk to existing or planned infrastructure.

2.2 Introduction and Motivation

Effective disaster risk management (DRM) requires accurate and up-to-date models [17, 81]. In many cases, DRM and supporting information comes from multiple disaggregated and potentially out-of-date sources that may not reflect the currently built environment [17, 78, 91]. An increase in disaster risks is also being driven by population growth and rapid urbanization [15]. To encourage the use of an updated database that includes high-resolution features, we present a method based on small, low-cost drone imagery and adapted open-source tools to classify the built environment and use this information to model flood and other risks. Resource-limited communities will benefit from on-demand use of easily captured, low-cost, and high-resolution drone imagery to periodically update property and natural hazard risk information [12, 100].

This article presents new analytical tools to conduct aerial imagery-based assessments for mitigating risk to existing and planned infrastructure. The goals of this work were: (1) to produce a DRM solution using low-cost drones for data collection, 3D cadastre modeling with the drone data, and disaster risk quantification for buildings; (2) to quantify building risk by combining flood models with building classification using drone imagery. While the methods presented in this paper apply to flooding due to this historically being a prime contributor to property damage [21], similar methods can be used to assess other risk sources. These risk sources could include earth movement, such as erosion, or urban development that alters an existing natural hydrological response.

Accurate cadastre information, or datasets that define property boundaries and ownership,

are frequently lacking in the developing world [16]. The lack of property titles can lead to conflict and insecurity, which, in turn, leads to instability for a country [16]. The Director of Land Affairs in the Democratic Republic of the Congo recently stated that “drones facilitate the real-time collection and rapid updating of land data, compared with traditional methods” [14]. A few accurate ground reference points visible in drone imagery are all that is required to complete a detailed cadastre for a community.

The ability to capture high-resolution imagery with a low-cost drone is matched to recent developments in Artificial Intelligence (AI) that can rapidly classify an area for features and objects of interest as well as create a reconstructed 3D environment for modeling purposes [57, 89]. A fully convolutional neural network with Feature Pyramid Network architecture from the 2020 Open Cities AI Challenge hosted by the World Bank [60] can effectively classify buildings. The trained models from the challenge are available for download and we plan to further train these models for different locations. The resulting layer of identified features from the neural network can be used to build a flood model of an environment. OpenDroneMap is an efficient, open-source structure from motion (SfM) program used to produce 3D models from aerial imagery [22]. This software can additionally generate digital terrain maps (DTM) from the drone imagery. The outputs of these programs could be used to further classify buildings by condition with the use of observed roof type as a metric for construction quality.

Flood analysis using the Soil and Water Assessment Tool (SWAT) [7] is an efficient way to determine how flood events impact communities. SWAT accounts for terrain features, such as water flow to sub-basins caused by gradients, and land use including agricultural, developed, and undeveloped land. In the context of urban ecology, SWAT models can be used to show the beneficial effects of limited development to improve water uptake, which reduces flood height and volume.

2.3 Drone-Based Data Collection and Analysis

2.3.1 Motivational Forces in Disaster Risk Management

According to the World Bank, since 1980, more than two million people and over \$3 trillion have been lost to disasters caused by natural hazards, with total damages increasing by more than 600% from \$23 billion a year in the 1980s to \$150 billion a year in the last decade [15]. In many developing countries, disaster risk is not contextualized at the community level during the project-planning process. An example is a school in Afghanistan funded by the World Bank, shown in Figures 2.1 and 2.2, that illustrates the disastrous impact natural hazards can have on infrastructure if not mitigated during the project planning process. The satellite images in Figure 2.1 show the location of a school before and after flooding of the Amu Darya river in Balkh Province, Afghanistan in April 2018. The photo in Figure 2.2 shows the extent of the damage caused to the school by flooding. This example underscores the need to provide donors, governments, and communities in developing nations access to low-cost data collection and analysis tools to assess and minimize disaster risk in order to protect lives and investments.

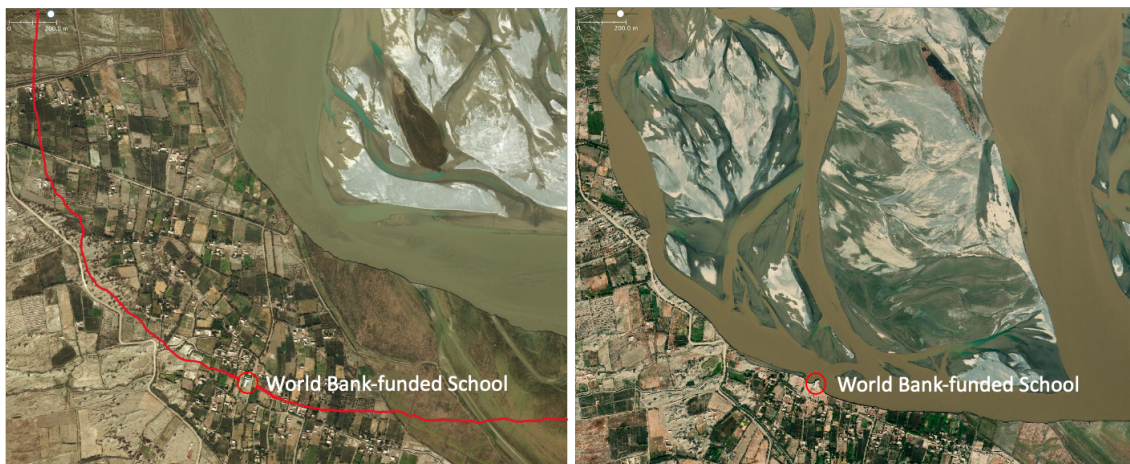


Figure 2.1: The location of a school in Afghanistan before and after a flood (Satellite imagery: ESRI). This flood of the Amu Darya river occurred in April 2018.



Figure 2.2: A school constructed in an Amu Darya river flood plain in Afghanistan and partially destroyed by flooding. This image was provided by Development Monitors LLC.

2.3.2 Down-Sized and Low-Cost Drone Technology

The drone market continues to evolve, with several small and low-cost drones now available on the consumer market. DJI is the world's largest consumer drone producer, with their products accounting for around 70 percent of the global consumer and enterprise drone market [13]. In addition to commercial drones for business, DJI also sells smaller and lower-cost drones, costing less than US \$500. A comparison of the three smallest DJI drones is shown in Figure 2.3.

The main advantage of sub-250 gram drones is that a country's regulatory authority may recognize the reduced operational risk for the low-weight aircraft, making access to airspace

easier [96]. Drones weighing less than 250 grams have inherently less kinetic energy, and therefore less injury and damage potential, making them appealing for flight operations in areas with higher population density.

Spark	Mavic Mini	DJI Mini 2
		
<ul style="list-style-type: none"> Small and Compact Quick Launch Obstacle Sensing 12 MP Camera Gesture Control QuickShot ActiveTrack 	<ul style="list-style-type: none"> 249 g Ultralight 30-Min Max. Flight Time 4 km HD Video Transmission Vision Sensor + GPS Precise Hover 3-Axis Gimbal 2.7K Camera Simplified Recording & Editing 	<ul style="list-style-type: none"> 249 g Ultralight 31-Min Max Flight Time 10km HD Video Transmission Vision Sensor + GPS Precise Hover 3-Axis Gimbal 4K Camera Simplified Recording & Editing
	USD \$399	USD \$449

Figure 2.3: A comparison of the three smallest drones produced by DJI. This comparison tool is available on the DJI website [59].

The use of a small, low-cost, and expendable drone can enable the inexpensive collection of high-resolution aerial imagery. The Virginia Tech Unmanned Systems Lab designed and assembled a custom drone from inexpensive, off-the-shelf components. This drone weighs less than 250 grams and is shown on a scale in Figure 2.4. The drone is made from a custom carbon fiber frame and uses a flight controller running ArduPilot software. The imaging system consists of a Raspberry Pi Camera V2 connected to a Raspberry Pi Zero board. The camera is pointed downward in a fixed direction with a vibration isolated mount and is capable of capturing 8 megapixel imagery [4].

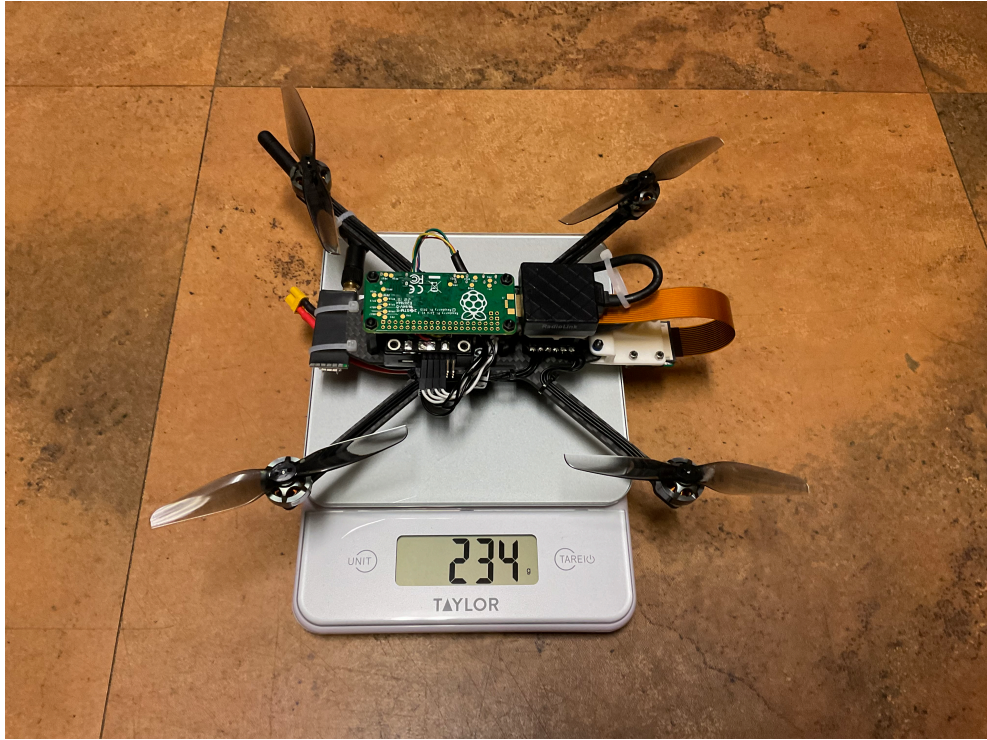


Figure 2.4: Our small, low-cost drone which weighs under 250 grams.

The drone is fully autonomous and flight plans are automatically generated using an application developed by the team. The planned mission covers a desired area while acquiring imagery that meets the required overlap and ground sample distance criteria. The planned mission is uploaded to the drone using the open-source Mission Planner software [86]. The drone is equipped with a telemetry radio for in-flight communication with an Android application also developed by the team.

Once the mission has been created and sent to the drone, no manual user intervention is needed other than a command to start the mission. The drone autonomously flies its mission and collects high-resolution imagery before landing. Due to the lack of required user input, missions with this drone can be performed by minimally trained operators, thereby enabling this system to be used by locals in communities throughout the world. The flight controller

includes fail-safe features where the drone will return to the home location and land in the event of a low battery or other issues during the mission. While the current drone does not include obstacle avoidance features, we hope to include these capabilities in a future version.

2.3.3 Machine Learning with Drone Imagery

Machine Learning techniques can be used on the high-resolution drone imagery in order to detect and classify objects and features. For our work, machine learning methods could be used to detect buildings, classify building roof type, and detect erosion patterns in the soil. Deep Neural Networks, or Artificial Neural Networks (ANN) with multiple layers, are considered one of the most powerful machine learning tools and have become very popular [46]. The Convolutional Neural Network (CNN) is one of the most popular deep neural networks [46]. “A Convolutional Neural Network is a Deep Learning algorithm which can take in an input image, assign importance (learnable weights and biases) to various aspects/objects in the image, and be able to differentiate one from the other” [95]. CNNs have achieved excellent performance in machine learning problems, especially applications that deal with image data, computer vision, and in natural language processing (NLP) [46]. CNNs are composed of multiple layers of artificial neurons, which are mathematical functions to output an activation value by calculating the weighted sum of multiple inputs [58]. The behavior of these neurons will be defined by their weights and they are able to pick out various visual features when the pixel values of an image are used as an input to the neural network [58]. CNNs can be “trained” using labeled input data to update the weights of its neurons in order to improve performance [58]. A test dataset is then used to verify the accuracy of the CNN on data it has not seen before [58].

Many open source machine learning libraries exist for Deep Learning with CNNs. Two of

the most popular open source machine learning libraries are TensorFlow [9] and PyTorch [5]. In addition to these open source libraries, proprietary software systems are also available.

2.4 Data Collection and Registration

2.4.1 Cadastre Systems and Data

Municipalities in developed countries use a wide variety of cadastre systems to document property ownership. A good example is from Montgomery County, Virginia (Figure 2.5). In many areas, particularly in the United States, cadastral information can be found and downloaded freely online.

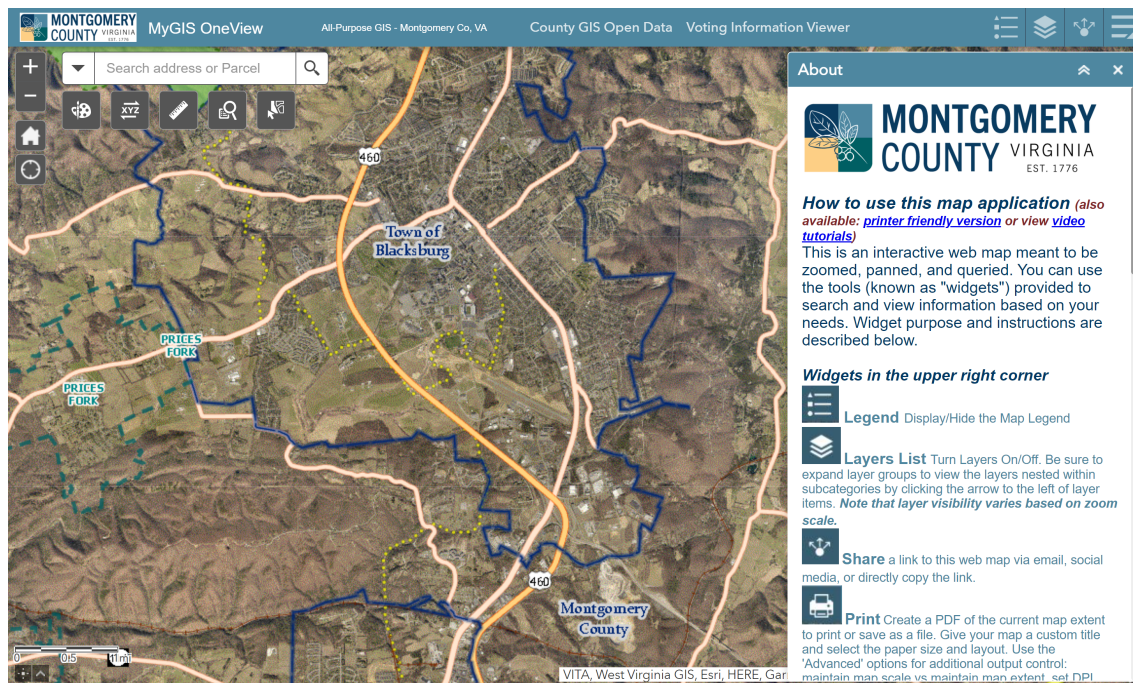


Figure 2.5: Sample cadastre system used in Montgomery County, VA, USA [2].

For the Commonwealth of Virginia, cadastral information is openly available on the Open Data Portal created by the Virginia Department of Transportation [24]. For our purposes,

shapefile, or GeoJSON formats of cadastral data can be displayed in GIS software such as QGIS [23] as shown in Figure 2.6. The figure shows data and satellite imagery for Kentland Farm, which is a farm that was acquired by Virginia Tech for research purposes. While cadastre data is openly available for much of the United States, this is not the case in many developing countries [16].



Figure 2.6: Property boundary data displayed in QGIS for the Virginia Tech Kentland research farm.

2.4.2 Natural Disaster Risk Applications and Data

Considerable effort in creating targeted and easy-to-implement disaster risk management (DRM) tools has resulted in a range of options for community planners. A good example is the Open HAZUS-MH tool [62] developed by the US Federal Emergency Management Agency (FEMA). This open-source risk modeling tool was developed for multi-hazard risk assessment in the US. As part of a World Bank project in Afghanistan, Development Monitors created a

natural disaster risk mapping plug-in for the open-source GIS application QGIS. The plug-in leverages available high-resolution imagery, multi-hazard natural disaster risk data, and a machine learning model to detect infrastructure features in order to create community-level disaster risk maps like the one shown in Figure 2.7. Multi-hazard risk data at the national and state levels are available to the general public from many sources, including FEMA, VFRIS, and others.

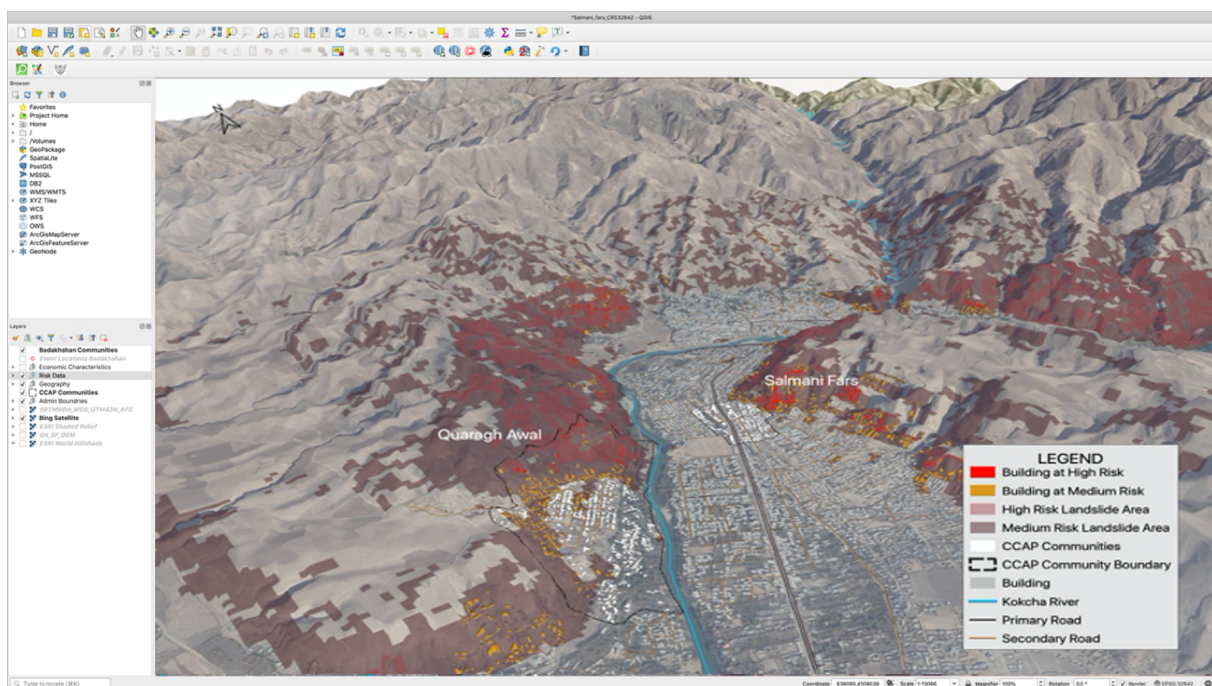


Figure 2.7: 3D landslide risk map of two communities in Badakhshan province, Afghanistan. This image was provided by Development Monitors LLC.

2.4.3 3D Modeling

Many different approaches are being explored for 3D visualization and 3D cadastral mapping and modeling. This includes the 3D cartographic visualization of a historical topographic object [98]. The use of surveyed ground control points, real-time kinematic positioning data, and Structure from Motion algorithms enable the generation of detailed 3D models of objects

and their surroundings with accuracy of up to several millimeters [98]. Models like this could be transferred and shared on public geospatial databases. Research is also being done on the use of modern game engines with geospatial data to create immersive virtual 3D environments for geographic visualization [72]. Additionally, significant research has been performed on the intersection of 3D cadastre data and building information modeling (BIM), which can provide a rich repository of legal and physical datasets in a common environment [47].

Using our drone system, we are able to collect high-resolution aerial imagery of properties. The collected imagery can then be post-processed to produce 3D reconstructions of an area. The open source OpenDroneMap software can be used to produce 3D textured models, point clouds, georeferenced orthorectified images, and georeferenced Digital Elevation Models from aerial imagery [22]. An example of a 3D reconstruction produced from aerial imagery collected by a small, low-cost drone is shown in Figure 2.8. While the georeferenced models can be produced using geotagged images, surveyed ground control points are needed to produce more accurate location data. Once the 3D models have been created, these can be combined with cadastre and risk data in order to further contextualize this information.



Figure 2.8: A 3D reconstruction produced from drone imagery captured at the Virginia Tech Kentland research farm.

2.4.4 3D Building Size Estimation

Aerial Building Segmentation

The georeferenced 3D models and point clouds constructed from drone imagery can be used to estimate the total volume and size of the buildings. Additionally, the constructed orthophoto can be used to detect the size and location of the building footprints. While object detection can determine the existence of a building, pixel-wise semantic segmentation is necessary to understand the true size and shape of the building. The performance of segmentation models can be summarized by three main metrics: Intersection over Union (IoU), Precision, and Recall. The IoU is calculated by dividing the area of overlap between the predicted bounding box and the ground-truth bounding box by the the area encompassed

by both the predicted bounding box and the ground-truth bounding box [94]. Precision is the fraction of relevant instances among the retrieved instances, which tells you how many of the detected buildings are actually buildings. Recall is the fraction of the total amount of relevant instances that were actually retrieved, which tells you how many of the actual buildings were detected.

I was able to leverage openly available building segmentation models from the “Open Cities AI Challenge: Segmenting Buildings for Disaster Resilience” [60]. The model uses a Feature Pyramid Network (FPN) with an efficient-net backbone and achieved an IoU of 0.84 on the challenge test set of buildings in Africa. This segmentation model was used on a drone image captured of the Dzaleka refugee camp in Malawi, which is shown in Figure 2.9. The original image is on the top left and the ground truth labels are shown below this. The image on the right shows the buildings which were detected by the segmentation model. This test image resulted in an IoU value of 0.824, a precision value of 0.933, and recall of 0.876.

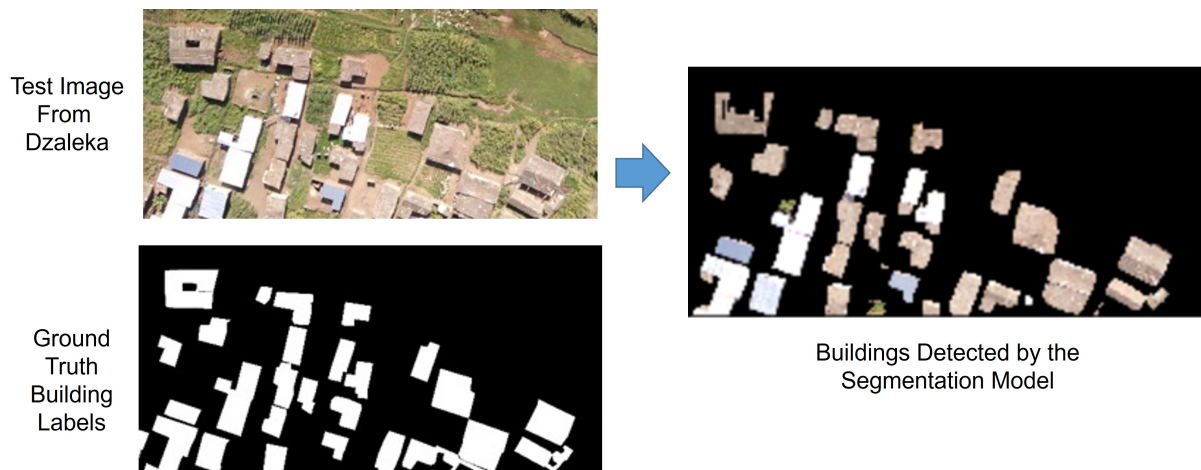


Figure 2.9: BUilding segmentation results for a drone image captured of the Dzaleka refugee camp in Malawi.

While the results were very good for the images in Africa, the goal at the time of this work was to be applied in Afghanistan. As a result, the segmentation model was then tested

on imagery captured of Afghanistan. Figure 2.10 shows the results of a test image from a rural area in Afghanistan. The segmentation model performed poorly on this image and was unable to detect many of the buildings.

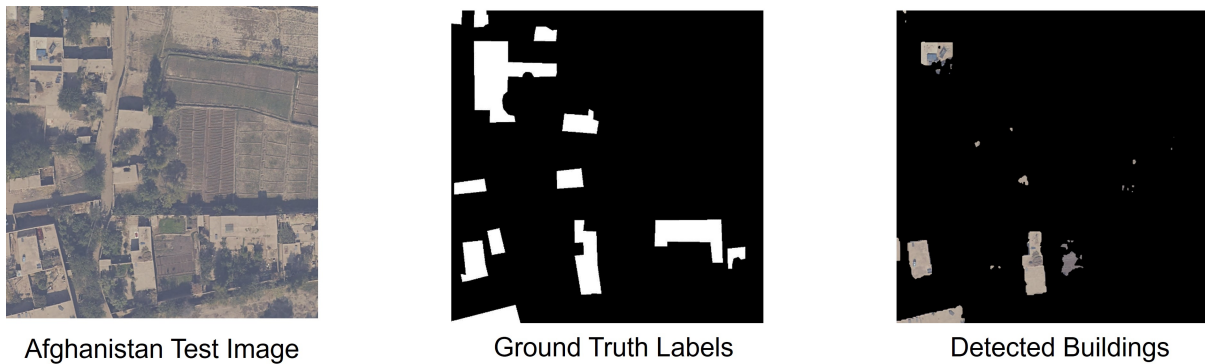


Figure 2.10: Segmentation results for an example test image of a rural area of Afghanistan.

The test area in Afghanistan contained many rural houses with mud roofs that appear similar to the ground. Due to this, the segmentation model performed poorly in rural areas relative to urban areas. Table 2.1 summarizes the model results for urban and rural areas of Afghanistan. The performance for urban areas was significantly greater than for rural areas.

Table 2.1: Accuracy results for the building segmentation performed on a test set of images from Afghanistan.

Areas	IoU	Precision	Recall
Urban	0.715	0.797	0.875
Rural	0.390	0.717	0.460

Due to the poor performance of the model for the rural areas of Afghanistan, retraining of the model was required to better detect the rural houses. Multiple iterations of retraining were performed to improve the detection accuracy in Afghanistan. Figure 2.11 shows an example of segmentation results before and after retraining. The original model achieved an IoU of 0.289 on this image, while the retrained model achieved an IoU of 0.687 for the same image.

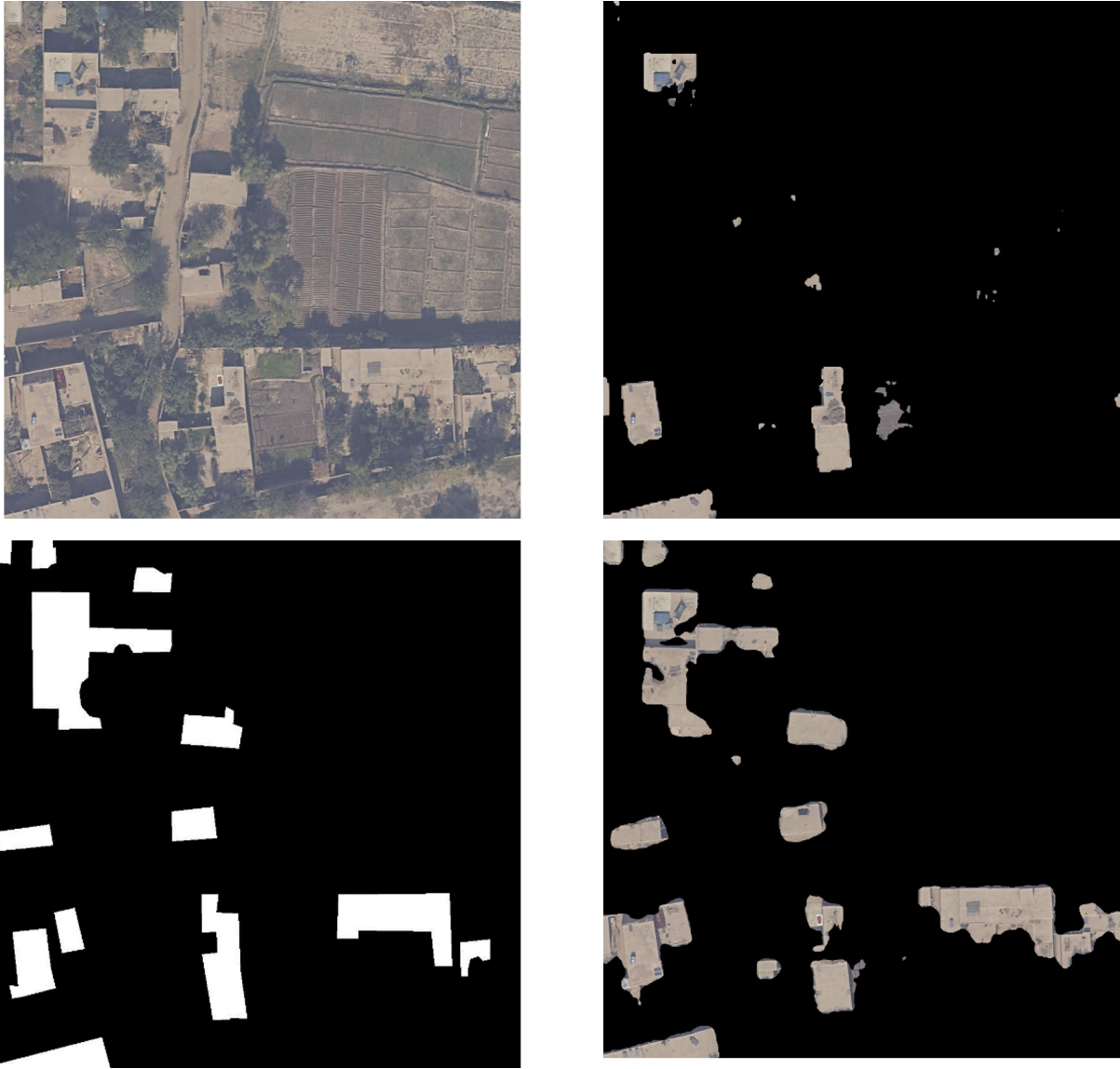


Figure 2.11: Segmentation results on a test image before and after retraining. The top left shows the original image with the ground truth labels on the bottom left. The top right image shows the detected buildings with the original model. The bottom right image shows the detected buildings with the updated models.

After training on the labeled dataset of images from Afghanistan, the model detection improved significantly for the desired test area. The segmentation accuracy results are summarized in Table 2.2 for the original model and two iterations of training. The IoU result for the test data set doubled while also significantly increasing both Precision and Recall.

Table 2.2: Accuracy results for the building segmentation performed on a test set of images from Afghanistan before and after training.

Model	IoU	Precision	Recall
Original	0.274	0.382	0.490
Version 2	0.516	0.760	0.617
Version 3	0.597	0.802	0.700

Facade Segmentation

While nadir drone imagery likely to be very accurate when estimating the building footprint, these images from above can provide less accurate estimates of the building height. In an effort to improve the accuracy of building height estimation, a building facade detection and size estimation algorithm was developed. The facade of a building can be detected using imagery facing the side of a building, taken from either the ground or with a drone in the air. Once detected, the building facades can then be used to estimate the area.

In order to perform segmentation to detect building facades, the DeepLabv3 architecture was used after being trained on the CityScapes dataset [55]. Figure 2.12 shows the segmentation results on two views of our lab building. The left images show the original image, the center image shows the segmentation results, and the right image shows the segmentation results overlaid on the original image. The labels for each color is shown on the far right. While the grass and sidewalks were not properly detected, the building class produced very accurate results.

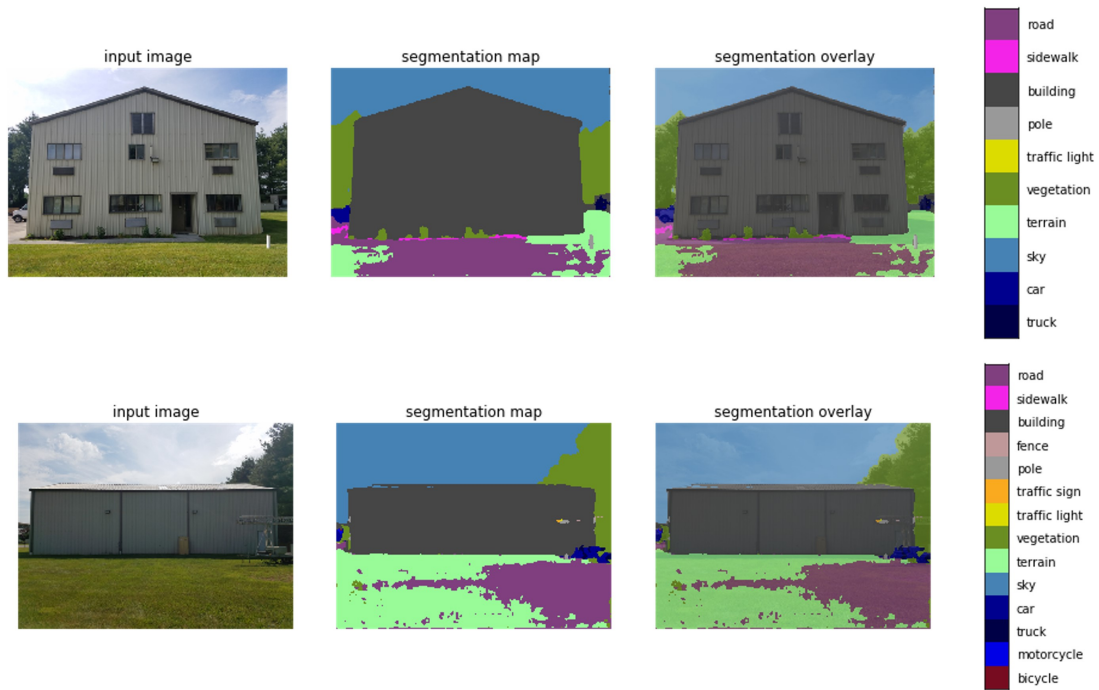


Figure 2.12: Two examples of building facade segmentation results.

After segmenting the building, OpenCV was used in order to create contours of the outline of the building facade. The detected contour of the building facade is then converted into an approximate polygon using the 'approxPolyDP' function in OpenCV. Figure 2.13 shows an example of this process. The original image is segmented in order to create a facade outline and polygon. The right image shows the overlay of the detected facade polygon and the actual facade polygon.

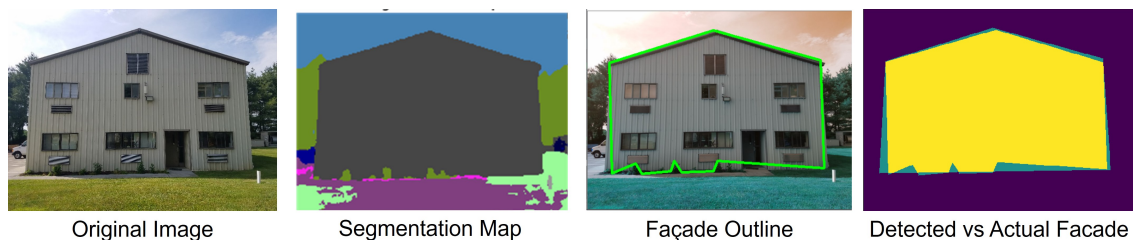


Figure 2.13: An example of the building facade segmentation and outline. The detected facade polygon is compared to the actual facade polygon in the right image.

An additional example of an image and the detected facade outline is shown in Figure 2.14.

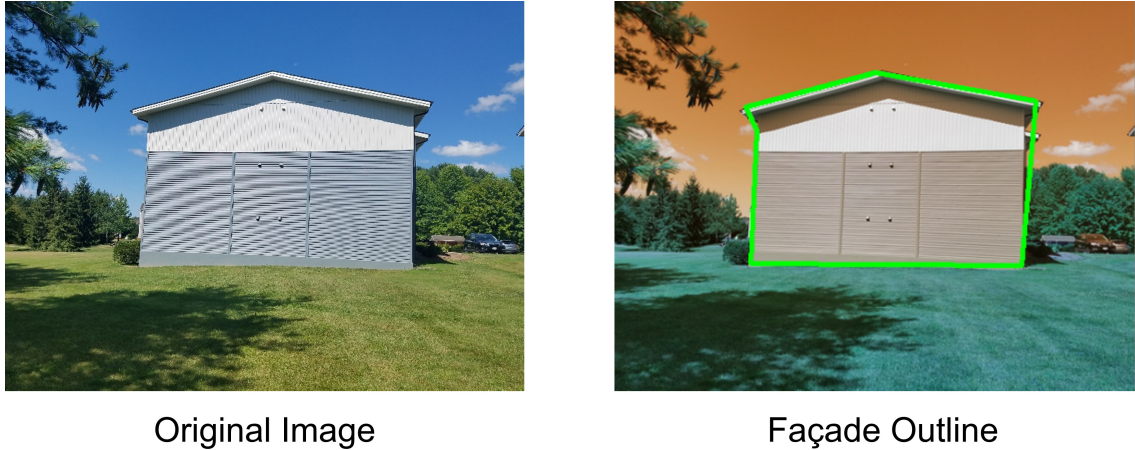


Figure 2.14: A second building facade detection example. The detected outline is overlaid on the original image in the image on the right.

Once the outline of the facade has been determined within the image, the camera focal length, sensor specifications, and the distance between the camera and the building are used in order to estimate the real-life height and area of the building facade. The following equations show the calculation to determine the real-life height and width of the image from the focal length of the camera and sensor specifications. In these equations, *Distance* is the GPS distance between the location of the camera and the location of the building facade, *f* is the focal length of the camera, *S_w* is the width of the camera sensor, and *S_h* is the height of the camera sensor.

$$ImageWidth = \frac{Distance * S_w}{f}$$
$$ImageHeight = \frac{Distance * S_h}{f}$$

From the real-life size of the full image, the size of the building facade within the image can then be calculated. Table 2.3 summarizes the Machine Learning Intersection over Union

(IoU), Machine Learning Facade Area percentage (pixel-wise), and the measured facade area error percentage in square meters for a test set of 25 images. This showed to be extremely accurate with Intersection over Union as well as the pixel-wise facade area detected. While the measured facade area was slightly less accurate, an error less than 7 percent is very good for an estimate of the building facade area. A significant contributor to the error for this could be due to errors in the calculated distance between the image and building resulting from errors in the GPS locations.

Table 2.3: Accuracy results for the building facade detection and size estimation.

Machine Learning IoU	Machine Learning Facade Area Error (%)	Measured Facade Area Error (%)
0.937	2.53	6.77

The combination of this facade size estimation technique and the aerial building footprint segmentation discussed earlier can produce accurate building volume estimates which can be then be used to estimate the property value when this data is not otherwise available.

2.4.5 Contextualizing 3D Models with Cadastre and Risk Data

In developing countries, drones coupled with a real-time kinematic (RTK) base station can enable communities to accurately create land registries [14]. In more developed countries, available cadastre and risk data can contextualize 3D models for mitigating risk at the property and building level.

After drone imagery has been processed by OpenDroneMap, georeferenced outputs can be aligned with and overlaid on top of property boundary data. The georeferenced orthorectified image, or orthophoto, of a building at Kentland Farm is shown in Figure 2.15. This orthophoto was overlaid on top of base satellite imagery and the property boundary data

using QGIS. The georeferencing was performed using the GPS data from the drone for each of the individual images. While the image aligns reasonably well with the satellite imagery, within a couple of meters, a GPS base station with ground control points would improve the georeferencing accuracy. Once the orthophoto and 3D model data have been aligned with the cadastre data, available risk data can contextualize this at the property and building levels to show the specific properties at risk. Disaster risk information can be highlighted within the property boundary and matched to specific portions of the 3D building data to clearly show how the buildings may be impacted.

Additional outputs of the drone image processing include DTMs. These can be produced by the open source OpenDroneMap software as well as many other proprietary software options. The use of a DTM as one of the inputs for risk assessment is discussed further in the following section.



Figure 2.15: A 3D reconstruction orthophoto produced from drone imagery captured at Kentland Farm overlaid on satellite imagery and cadastre data in QGIS.

2.5 Discussion and Conclusions

In this work, we present a concept of simplified data collection, 3D cadastre modeling, and natural disaster risk assessment through the use of low-cost drones and adapted open-source software. The complete solution architecture includes data collection with low-cost drones, 3D cadastre modeling with the drone data, and natural disaster risk quantification for buildings. To collect high-resolution aerial imagery, a small, low-cost, and autonomously flown drone was developed. The collected aerial imagery can be used to produce 3D cadastre models in order to contextualize and quantify potential natural disaster risk to infrastructure and property through the addition of natural disaster risk data. The aerial imagery is first

processed to produce georeferenced 3D reconstructions, digital elevation models, and orthomosaics. These can be combined with cadastre data in order to produce 3D cadastre models. While many studies have used 3D visualization and drone imagery with cadastre modeling and mapping [11, 47, 52, 98], our work additionally processes the drone imagery to help determine risk data so that this can be contextualized with the 3D cadastre. While our risk assessment work has focused on flood modeling, the collected data can be used to assess and contextualize many other potential natural disasters as well. Future work will need to be done to overlay the risk data on the 3D cadastre models. The combined risk and 3D cadastre data can help pinpoint exactly how specific buildings may be impacted. With flooding, for example, the 3D visualization would enable possible flood depth to be understood relative to the height of the buildings.

Chapter 3

Post-Flood Analysis for Damage and Restoration Assessment Using Drone Imagery

This chapter was previously published in the journal *Remote Sensing* with the title "Post-Flood Analysis for Damage and Restoration Assessment Using Drone Imagery" [107]. All work in this chapter was performed by me, except for Section 5, which was performed by Kunal Joshi.

3.1 Abstract

With natural disasters continuing to become more prevalent in recent years, the need for effective disaster management efforts becomes even more critical. Specifically, flooding is an extremely common natural disaster which can cause significant damage to homes and other property. In this article, we look at an area in Hurley, Virginia which suffered a significant flood event in August 2021. A drone is used to capture aerial imagery of the area and reconstructed to produce 3-dimensional models, Digital Elevation Models, and stitched orthophotos for flood modeling and damage assessment. Pre-flood Digital Elevation Models and available weather data are used to perform simulations of the flood event using HEC-

RAS software. These were validated with measured water height values and found to be very accurate. After this validation, simulations are performed using the Digital Elevation Models collected after the flood and we found that a similar rainfall event on the new terrain would cause even worse flooding, with water depths between 29% and 105% higher. These simulations could be used to guide recovery efforts as well as aid response efforts for any future events. Finally, we look at performing semantic segmentation on the collected aerial imagery to assess damage to property from the flood event. While our segmentation of debris needs more work, it has potential to understand the extent of damage and aid disaster response. Based on our investigation, the combination of techniques presented in this article has significant potential to aid in preparation, response, and recovery efforts for natural disasters.

3.2 Introduction

Between 1970 and 2019, the number of natural disasters has increased by a factor of five, driven by climate change, more extreme weather, and improved reporting [26]. In the 20 year period between 1995 and 2015, flooding was the most common natural disaster by a wide margin [83]. A joint report by the UN Office for Disaster Risk Reduction and the Centre for Research on the Epidemiology of Disasters recorded 3,062 natural flood disasters, which accounted for for 43% of all recorded events in this 20 year period [10, 83]. This was brought into the spotlight again recently with a catastrophic flood event occurring at Yellowstone National Park in June 2022 [40, 41]. According to the USGS, the Yellowstone flood could be considered a 1 in 500 year event since peak streamflow was higher than the 0.2% (or 1 in 500) flood [42]. The extreme nature of the flood underscores an increasing trend in extreme weather events. Due to the significance of flood events, our work focuses

on flooding. Specifically, we look at a test case of a devastating flood which occurred in Hurley, Virginia in 2021.

When responding to any disaster, three resources are particularly vital: money, time, and supplies [84]. Depending on circumstances and location, emergency response to a natural disaster may not be as effective. This is particularly the case if multiple simultaneous disasters put a strain on much-needed resources [84]. The first 72 hours after a disaster are especially crucial and response must occur during that time to save lives [87]. After the initial response stage, recovery efforts are necessary to rebuild the impacted community. Additionally, preparedness is vital since more preparation beforehand will improve the response to a disaster [87]. This preparation can be done before any disaster occurs and during recovery and rebuilding efforts after a disaster.

Drones are becoming increasingly used in disaster management or humanitarian aid [80]. Unmanned aerial vehicles (UAVs), which are more commonly known as drones, are aircraft without any humans onboard. The use of drones enables the possibility for quickly surveying and collecting data after a natural disaster. Aerial imagery from drones is widely used for producing extremely detailed 3-dimensional models and Digital Elevation Models of the terrain. Since managing floods is a very complex and difficult task which requires continuous monitoring of specific areas, drones could be helpful for keeping an area under observation [92]. Based on a search of other research papers, the most common drone application in disasters has been for mapping or disaster management [80]. The majority of studies have been focused on drone-based support of mitigation and recovery activities, while there is a lack of response-related research [73]. Based upon their comprehensive study of articles on remote sensing of natural hazard-related disasters, Kucharczyk and Hugenholtz recommend additional research and future studies be performed on earthquakes, floods, and cyclones/windstorms along with in-depth damage assessment for recovery, among other ar-

eas. Some work has been performed for disaster response and damage assessment using drones, with one specific case study looking at flood damage in Malawi [108, 114].

In this work, we look at a specific flood event in southwest Virginia in 2021. Aerial imagery is collected using a drone over portions of the area. This data is then used to create point clouds and digital elevation models. Using digital elevation models from before the flood, weather data, and measured water heights, we validate flood simulations of the event. After validating these simulations, we look at how another similar weather event would impact the new terrain. This is examined with the goal of using this data to aid recovery and preparedness of future events, which will also help aid disaster response efforts if another natural disaster strikes. Finally, we use semantic segmentation on the aerial imagery in order to analyze the amount of damage which was sustained during the flood event.

3.3 Materials and Methods

3.3.1 Test Area

The test area used for this work was a portion of Guesses Fork Road in Hurley, Virginia. Hurley is a small community in Southwest Virginia very near to the Kentucky and West Virginia state lines. On August 30, 2021, heavy rainfall caused significant flooding, landslides, and mudslides in Hurley. This resulted in the destruction of over 20 homes and led to death of one person [82]. The flooding in this area occurred rapidly in a short time frame, with water rising up and in people's homes in less than 30 minutes [75]. Rainfall estimates varied around the area, but over six inches of rain was estimated to have fallen along portions of Guesses Fork Road [25]. Within the first two days of emergency response, emergency personnel estimated they had conducted between 40 and 50 evacuations [74]. In the immediate

aftermath of the flooding, officials estimated that it could take a month before electricity was restored and a year before water service would be restored in the affected communities [102]. Despite the devastation in the area, the Federal Emergency Management Agency (FEMA) denied the request of Individual Assistance to those impacted by the flooding [82]. This further highlights the necessity of the development of rapid assessment techniques which can quantify the magnitude and likely recurrence of natural disasters.

3.3.2 Test Area Data Collection

In order to collect imagery of the test area after the flood damage, two visits were made to Hurley: one in November 2021 and the second in April 2022. During our two visits to the flood site in Hurley, a DJI Mavic Air 2 drone was used for collecting aerial imagery. The left portion of Figure 3.1 shows a map of Virginia and surrounding states with the location of Hurley marked by a pin. The right portion of the figure shows a picture of a DJI Mavic Air 2 drone, which was the model of drone used for our data collection. Flights were performed at an altitude of 50 meters with the camera set to capture 12 megapixel nadir imagery. During the first visit in November, six flights were flown to collect imagery over the flooded areas. Five additional flights were flown along the same stretch of road during the second visit to the area in April.

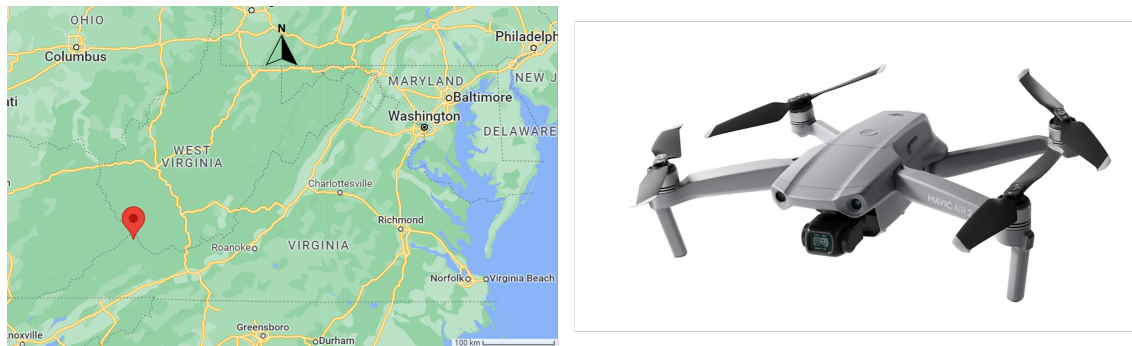


Figure 3.1: A map with a pin marking the location of Hurley, VA is shown on the left. The right portion shows a DJI Mavic Air 2 drone [32], which was used to capture imagery at the test area in Hurley.

For flood analysis of the test area, weather data was needed from the flood event on August 30, 2021 along with terrain data from before the flood event. Terrain data for this area was acquired from the Virginia LiDAR Inventory Web Mapping Application [39]. This portal for open data includes LiDAR point clouds and Digital Elevation Models obtained from NOAA (National Oceanic and Atmospheric Administration), USGS (United States Geological Survey), and VGIN (Virginia Geographic Information Network) data portals. For our flood analysis, the Digital Elevation Models were used. These were last updated in 2016, which was five years before the flood event. As a result, we are assuming the terrain along the road did not significantly change between when the DEMs were produced and the flood in 2021. A portion of one of these sections of the Digital Elevation Model is shown in Figure 3.2.

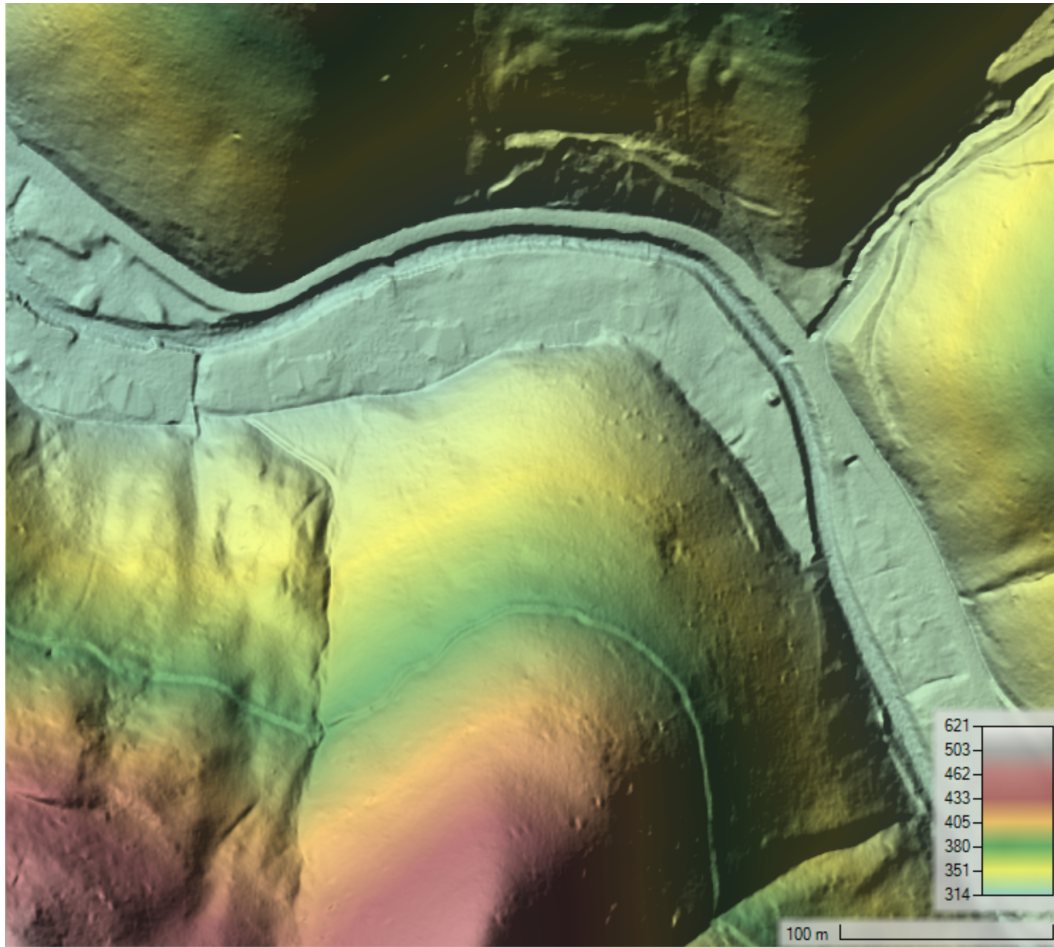


Figure 3.2: Digital Elevation Model of a small section of Guesses Fork Road in Hurley, Virginia.

Rainfall data was acquired from the NOAA National Severe Storms Library (NSSL) Multi-Radar/Multi-Sensor System (MRMS) [33]. "The Multiple Radar Multiple Sensor system combines data streams from multiple radars, satellites, surface observations, upper air observations, lightning reports, rain gauges and numerical weather prediction models to produce a suite of decision-support products every two minutes" [34]. Rainfall data is available in Radar only and Multi-Sensor QPE (Quantitative precipitation estimation). Radar only QPE values are precipitation accumulations derived from the summation of the Surface Precipitation Rate (SPR) product over specific time intervals [37]. Multi-sensor QPE uses a

combination of gauges and Numerical Weather Prediction (NWP) Quantitative Precipitation Forecasts (QPF) to fill in gaps in poor radar coverage areas [36]. The Multi-sensor QPE values were used as the precipitation for our simulations since this should be more accurate than radar only data. The Multi-sensor QPE data is available at 1 hour intervals, so this interval was selected for our simulations. An example of the product viewer containing precipitation data is shown in Figure 3.3.

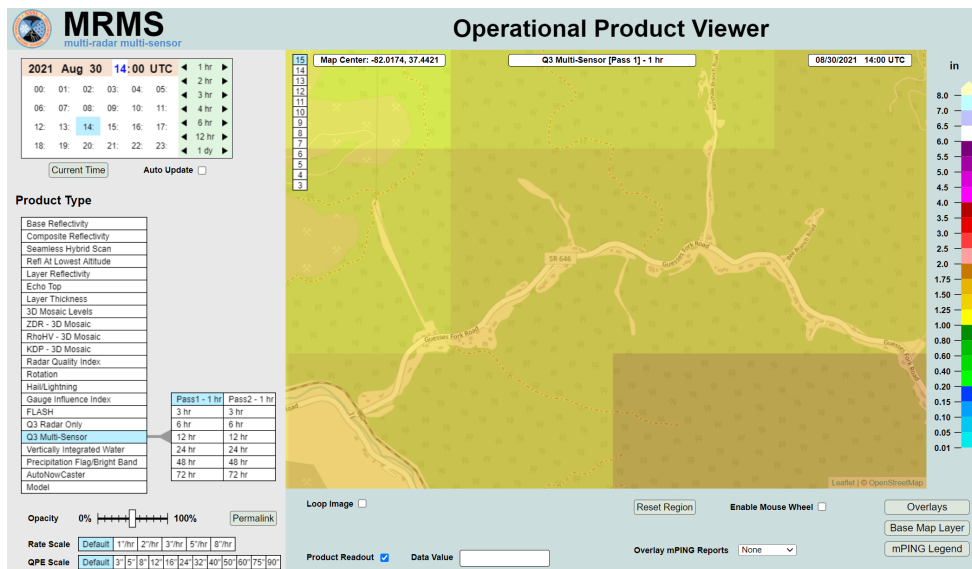


Figure 3.3: Example Multi-sensor Quantitative precipitation estimation data for the Guesses Fork Road area of Hurley, Virginia. The data is being displayed in the Operational Product Viewer [35].

The MRMS system also contains streamflow values calculated using the rainfall observations. The Flooded Locations And Simulated Hydrographs Project (FLASH) [27] has produced many flood prediction products, including a maximum streamflow value at each grid point. The products for streamflow include 3 models for calculating these values: CREST, SAC-SMA, and Hydrophobic [38]. For our simulations, we used the CREST (Coupled Routing and Excess Storage) distributed hydrological model data. CREST was jointly developed by the University of Oklahoma and NASA SERVIR to "simulate the spatial and temporal

variation of land surface, and subsurface water fluxes and storages by cell-to-cell simulation” [105]. The CREST flow values are available at 10 minute intervals, but hourly values were used to match the rainfall data interval.

3.3.3 Image Reconstruction Software

After collecting aerial imagery of the test area, this data was processed using OpenDroneMap to produce point clouds, orthorectified imagery, and Digital Elevation Models. OpenDroneMap is an open source toolkit for processing aerial imagery [22]. OpenDroneMap can be used to turn simple 2D images into classified point clouds, 3D textured models, georeferenced orthorectified imagery, and georeferenced Digital Elevation Models [18]. Structure from Motion (SfM) techniques are utilized to generate the 3-dimensional data from 2-dimensional imagery. The ODM software is available for Windows, Mac, and Linux and can be run using native installation or through docker [18].

3.3.4 Flood Analysis Software

For flood analysis, we are using HEC-RAS (Hydrologic Engineering Center’s River Analysis System) to perform the simulations. HEC-RAS is an open source software which allows users to perform one-dimensional steady flow, one and two-dimensional unsteady flow calculations, sediment transport and mobile bed computations, and water temperature and water quality monitoring [28]. HEC-RAS has been used and analyzed in many different studies for flood mapping, including in Italy and Kazakhstan [56, 88].

3.3.5 Workflow

A general workflow for our application of drones for the post-flood response and recovery is outlined in Table 3.1. The first step should begin as soon as possible to begin capturing aerial imagery during the critical first 72 hours. A drone and a certified pilot are required for this imagery collection portion of the workflow, with the time required depending on the size of the disaster area. Once imagery has been collected, it can be reconstructed to produce 3D models and digital terrain data. With an experienced user, this portion can be performed in a matter of hours. The time is also dependent on the amount of imagery and computer hardware to run OpenDroneMap. The next steps, damage segmentation and flood analysis, can be performed simultaneously if the necessary resources are available. If proper trained models exist, damage segmentation can be performed relatively quickly to understand the true extent of damage. Without this, manual inspection of the data would be much more time-intensive. Flood analysis using post-disaster imagery can be useful for guiding restoration efforts and determining future risks of major flooding. If a community keeps updated aerial imagery before a disaster, this flood modeling analysis could additionally be used to prepare for damage which may be expected during an upcoming flood.

Table 3.1: General workflow for our flood response and recovery tools.

Step	Task	Resources	Time
1	Post-disaster Aerial Imagery Collection	Drone, Pilot	1 day
2	Reconstruct Aerial Imagery	Drone Imagery, OpenDroneMap, User	2-5 hours
3	Damage Segmentation	Drone Imagery, Trained Segmentation Models, User	1-3+ days
4	Post-disaster Flood Analysis	Terrain Data, Precipitation Data, User	1-3+ days

3.4 Drone Image Reconstruction

3.4.1 OpenDroneMap Reconstructions

The drone imagery collected during our two trips to Hurley were processed using OpenDroneMap to produce 3D point clouds, georeferenced orthophotos, and Digital Elevation Models. Example 3D textured meshes produced from our drone imagery are shown in Figures 3.4 and 3.5. These two figures show 3D views of the area which flooded. Figure 3.4 shows an area where several buildings were damaged during the flood event. A portion of the stream can be seen to now flow directly into a building near the center of the image. One of these houses was even moved from its foundation during the flood event. Figure 3.5 shows a different portion of the Guesses Fork Road area, which was reconstructed using the drone imagery collected during our second trip to Hurley in April. In this portion, while damage is still present, some recovery efforts to the area can be observed as well. For example, a new bridge has been built over the stream near the center of this image. Next to this new bridge, the previous bridge can be seen at the bottom of the stream.



Figure 3.4: 3D reconstruction of a portion of Guesses Fork Road in Hurley, Virginia.



Figure 3.5: 3D reconstruction of a portion of Guesses Fork Road in Hurley, Virginia.

3.4.2 Comparison and Interpretation of Visual Data

Figures 3.6 and 3.7 show comparisons of satellite imagery from before the flood event to the orthophotos created from the aerial imagery collected with our drone. These two comparisons were selected to highlight some of the damage which occurred in this area during the flooding. In Figure 3.6, the stream has become much wider in this portion due to a noticeable amount of erosion to the land around the stream. Additionally, the bridges from the road to the homes were destroyed and washed away during the flooding. While the buildings in this area were not destroyed or washed away, the flooding had an observable impact on the terrain surrounding these buildings. Figure 3.7 shows an example of a location where homes were completely destroyed during the flood. Changes to the stream size in this area are not as dramatic, but multiple buildings and many trees in this area were wiped out.



Figure 3.6: A comparison of pre-flood satellite imagery to post-flood imagery. The image on the left shows Google Maps satellite imagery. The image on the right shows the post-flood orthophoto overlaid on the satellite image in GIS (Geographic Information System) software.



Figure 3.7: A comparison of pre-flood satellite imagery to post-flood imagery. The image on the left shows Google Maps satellite imagery. The image on the right shows the post-flood orthophoto overlaid on the satellite image in GIS software.

3.5 Flood Simulations

3.5.1 HEC-RAS Flood Event Simulation

By using HEC-RAS software, flood simulations were performed for multiple sections across the flooded area. Two-Dimensional unsteady flow modeling was performed in HEC-RAS to simulate the flood event which occurred. Since our drone imagery was collected over several small and disconnected sections along the road, flood simulations were performed on the areas corresponding to where the imagery was collected. As a result of these small simulation areas, very small cell sizes were required to grid these simulation areas. The 2-D mesh for the simulations used 1 meter by 1 meter cell sizes to grid the area. Due to this very fine discretization, careful selection and adjustment of the simulation time step was required to ensure a stable numerical analysis. HEC-RAS includes a variable time step option, which uses the Courant number to adjust the time step [31]. Maximum and minimum values can be set for the Courant number threshold using this method. For some cases, a stable and accurate solution could be achieved with a Courant number as high as 5, but more rapid changes of depth and velocity require a maximum Courant number closer to 1 [29, 31]. A maximum Courant number of 1 was set for our simulations, which resulted in stable solutions even with the fine discretization of the mesh.

The Manning's Roughness Coefficient, also known as Manning's n Value, is an important parameter for HEC-RAS simulations. The roughness coefficient can be set for a simulation using land cover data [30]. The USGS National Land Cover Database (NLCD) provides descriptive data for characteristics of the land surface [69]. These classes of land cover include multiple types of forests and crop lands, barren land, open water, and developed land. The developed land classes include open space, low intensity, medium intensity, and high intensity. The developed areas are considered those which contain a mixture of constructed materials

and vegetation and the different developed land classes are defined by the percentage of total cover which impervious surfaces account for [3]. Much of the development along our area of interest would be considered Low Intensity, since impervious surfaces account for between 20% to 49% percent of total cover. Areas with impervious surfaces accounting for less than 20% are classified as Open Space. The HEC-RAS user's manual suggests roughness coefficient values between 0.03 and 0.05 for Developed, Open Space and values between 0.06 and 0.12 for the Developed, Low Intensity class [30]. For the specific test areas presented in this paper, the land cover was classified on the lower end of the Developed, Low Intensity class. As a result of this, a roughness coefficient value of 0.06 was selected for these areas.

The Multi-sensor QPE data was used as the precipitation input across the 2-D mesh for the simulations. A plot of this precipitation data is shown in Figure 3.8 for one of the simulations. The plot shows hourly precipitation accumulations over the simulation time period. All of our simulations were run using a 48 hour time period between August 30, 2022 at 12:00 am UTC and September 1, 2022 at 12:00 am UTC. Rainfall and water flow values were collected hourly across this 48 hour period of time.

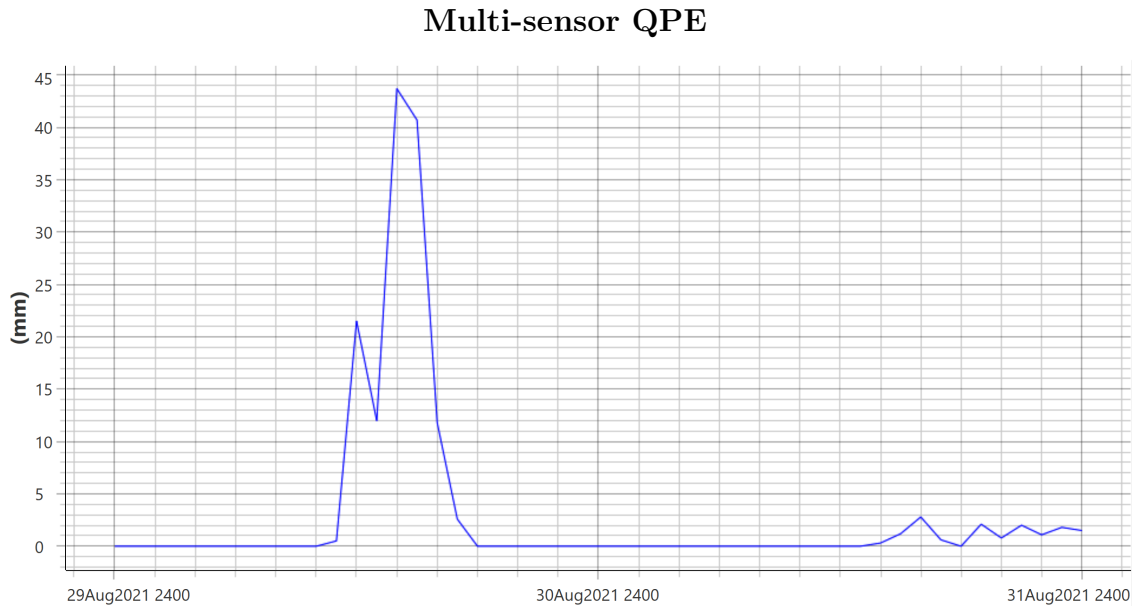


Figure 3.8: Multi-sensor Quantitative precipitation estimation data for one portion of Guesses Fork Road.

The inlet boundary condition for the 2D hydraulic model used a flow hydrograph with the data taken from the CREST flow product described above. The outlet boundary conditions was set to Normal Depth since this setting is a standard option which doesn't require as much data. The water volume accounting error percentage in HEC-RAS for the first simulation was 0.044%, while the second simulation was higher, with a value of 0.47%. The water depth output from HEC-RAS for the first simulation is shown in Figure 3.9. The deepest values are seen along the stream, with water depths of more than one meter also spreading into the surrounding land. The location of our ground-truth measurement location is marked on the image. The ground-truth measurements are discussed in the following section.

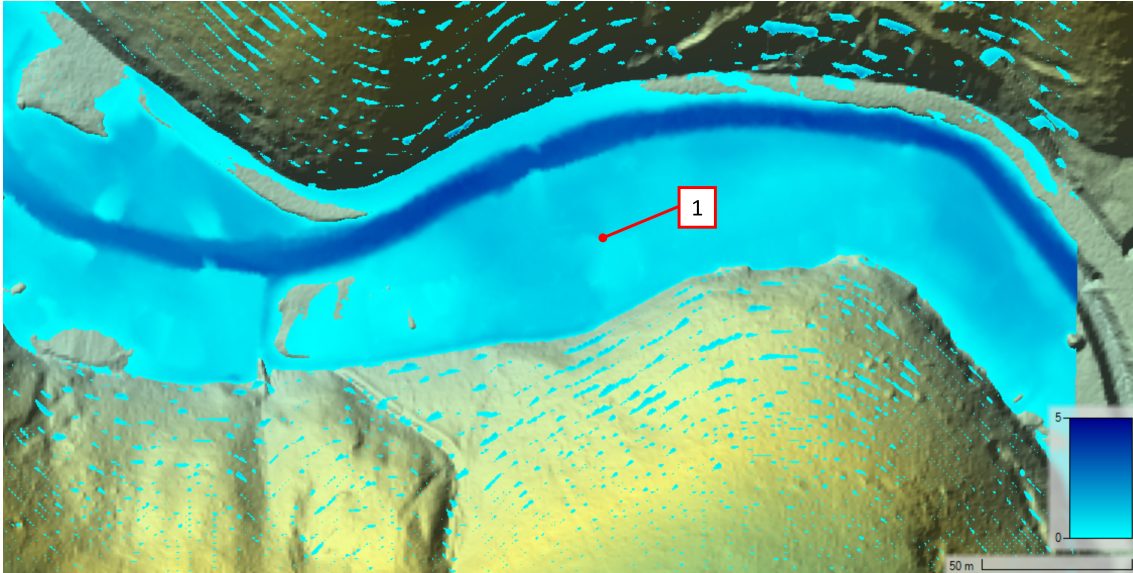


Figure 3.9: HEC-RAS simulated water depth values using the Digital Elevation Models from the Virginia Lidar dataset. This represents the terrain before the flooding event occurred.

3.5.2 Flood Water Depth Accuracy

Ground-truth water depth measurements were acquired during our visit by using the water lines observed on houses and trees. Three ground-truth measurements were used for comparison to verify the accuracy of the flood simulations for two different sections of the area. For each ground-truth measurement location, three different measurements were taken within a 0.3 meter diameter to determine the water depth values. These three measurements were averaged at each location to determine an average water depth value at each ground-truth location. Variations in the measurement values at each location were only a couple of centimeters, resulting in small standard deviations for these measurements.

To assess the accuracy of the HEC-RAS flood simulations, multiple measurements were taken of the flood depth based on marks left after the flood. Figures 3.10 and 3.11 show the locations of three measurements taken at the flood site. These two figures show the flood

locations labeled on the orthophotos and satellite imagery. The first measurement location, shown in Figure 3.10, was at one of the buildings. A large quantity of mud entered this house and covered portions of the floor at depths of over 0.3 meters. Using water lines left in the house from the flood, the water depth was measured to be 1.35 meters above the ground at this location. The second water depth measurement location is shown in Figure 3.11 and was measured to be 2.51 meters above the streambed. This measurement was taken along the stream, next to the road at an area where drone imagery was collected. The third water depth location is also shown in Figure 3.11 on top of satellite imagery. A measured water depth of 3.4 meters was measured at the location where a railroad bridge crosses over Guesses Fork Road.



Figure 3.10: The first flood depth measurement location marked on an orthophoto overlaid on satellite imagery. This measurement was taken at one of the houses along Guesses Fork Road.



Figure 3.11: The second and third flood depth measurement location marked on an orthophoto overlaid on satellite imagery. The second measurement was taken along the stream, next to the road. The third measurement was taken at the railroad bridge at the end of the road.

The water depth accuracy from the simulations is summarized in Table 3.2. In the first simulation, one water depth measurement was taken from a building which was flooded. This first value was at measurement location 1, with a measured water depth of 1.35 meters above the ground. The HEC-RAS simulation produced a value of 1.32 meters, which is an error of only 2.22%. The second simulation included two measured water depths from this area, locations 2 and 3 from Figure 3.11. The simulation values produced an error 8.37% and 2.06% for locations 2 and 3, respectively. These values validated that our simulations very accurately represented the water flow of the actual flood event. While one of the locations had an error over 5%, within 10% was still deemed to be acceptable. Some error could be inherent due to the pre-flood event terrain data being several years old. Although these

simulations were very accurate, they could be potentially improved by including sediment flow in our HEC-RAS simulations. Without any sediment flow element, our simulations do not account for the landslides which occurred during the flood event.

Table 3.2: A comparison of the water depth from the HEC-RAS simulation and the measured values during our visit to Hurley.

Measurement Location	Simulated Water Depth (m)	Measured Water Depth (m)	Error (%)
1	1.32	1.35	2.22
2	2.30	2.51	8.37
3	3.33	3.40	2.06

3.5.3 HEC-RAS Simulation on Post-Flood Environment

After the HEC-RAS simulation for the flood event was validated with the ground-truth measurements, additional simulations were run on the post-flooded environment using the same input rainfall data. This allows us to investigate additional risk to these area for future floods after restoration of the stream environment. In order to examine the restoration impacts at our test area in Hurley, we performed flood simulations in HEC-RAS using Digital Elevations Models produced from drone imagery collected after the flood, which were discussed in Section 3.4. The same precipitation input and flow boundary conditions were used for this simulation as the simulations performed on the pre-flood environment. This allows us to examine how the same rainfall event would impact the new terrain compared to the effects of the August flood event. Figure 3.12 shows the HEC-RAS simulated water depth results using the post-flood Digital Elevation model of the same area as the simulation in Figure 3.9.

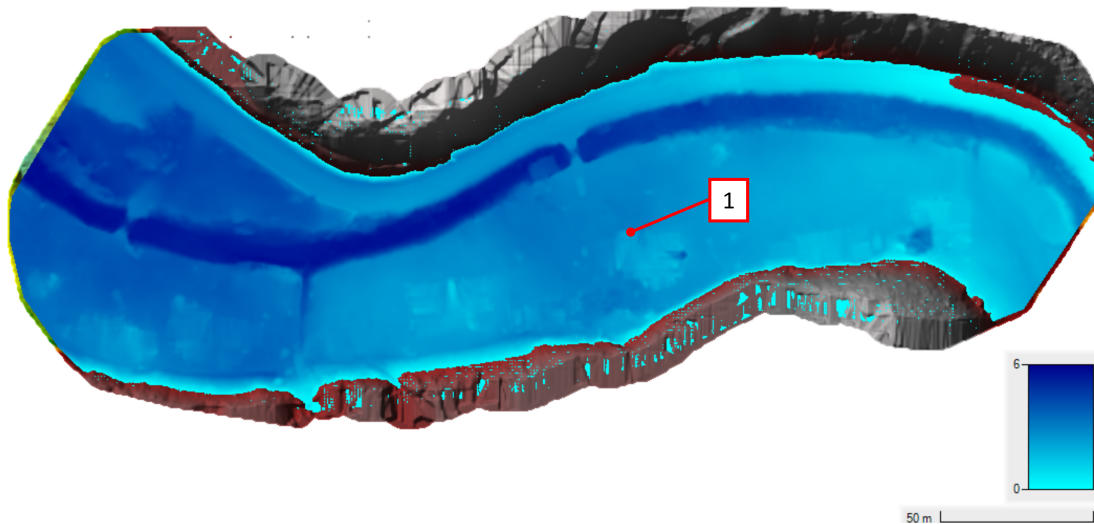


Figure 3.12: HEC-RAS simulated water depth values using a post-flood environment Digital Elevation Model. This is the same area as the simulation in Figure 3.9.

Table 3.3 shows a comparison of the simulated flood depth values for the pre-flood environment and the post-flood environment. Water depth values were calculated for measurement locations 1 and 2. Measurement location 3 was outside of the area we captured imagery of with our drone, so we were unable to perform a flood simulation using post-flood terrain of this area. The flood depth values were calculated relative to static ground locations, which were assumed to have not moved. The first location water depth was measured from the ground outside of a house, which did not move during the flood event. The second depth measurement was taken relative to the streambed, which was observed to not have a large amount of debris or sediment buildup in this area. At the first measurement location, the simulated flood depth doubled when using the post-flood terrain compared to terrain from before the flood. While the second measurement location saw a 29.1% increase in water depth for the post-flood terrain.

Table 3.3: A comparison of the water depth from the HEC-RAS simulation using pre-flood and post-flood terrain.

Measurement Location	Pre-flood Water Depth (m)	Simulated	Post-flood Water Depth (m)	Simulated	Depth Change (%)
1	1.32		2.7		105
2	2.30		2.97		29.1

3.6 Damage Analysis Using Semantic Segmentation

Use of computer vision techniques to analyze disaster damage is becoming more popular due to developments in Computer Vision algorithms and cost effectiveness of UAV mapping [53, 90, 109, 110, 113]. Semantic segmentation is one of the most important and extensively studied tasks in Computer Vision. In semantic segmentation, we assign class label to each pixel in an image. With the recent developments in autonomous driving, medical imaging, and face recognition systems, more robust segmentation and object detection models have been developed, especially using Deep Learning. Convolutional Neural Networks (CNNs) use filter operations to find spatial and temporal dependencies in images and they are widely used for object detection, classification and segmentation. Fully Convolutional Networks (FCN) [97] replace the fully connected layer in image classification neural networks with convolutional layers for semantic segmentation. U-Net [93] uses encoder-decoder network with skip connections for context information. PSPNet [112] uses feature pyramid pooling with atrous convolutions to get global context information. DeepLabV3+ [51] uses both atrous spatial pyramid pooling and encoder-decoder architecture.

Despite all this development in semantic segmentation and computer vision, there is a shortage of low altitude, high resolution annotated images for UAV disaster damage analysis. RescueNet [53] contains images of Hurricane Michael. Annotations for 11 classes including

road, damaged and undamaged buildings, vehicle, water, etc. are provided in RescueNet. This dataset is a great resource for disaster damage analysis with semantic segmentation. Our work is similar to this work except that we focused more on analyzing the debris. Additionally, RescueNet lacks good annotations for debris class. We believe that analysis of debris distribution can potentially provide a new insight in predicting, mitigating, and responding to disaster damage. ISBDA [113] provides a building damage analysis in three categories: slight, severe, and debris. But this dataset does not have other classes such as road, water, and vehicles which are crucial for Search and Rescue (SAR) missions. Other research in this area, such as [66], used texture analysis on UAV images and showed that HOG (Histogram of the Oriented Gradient) filters can be effectively used in disaster debris identification. [104] used Bag-of-words (BoW) feature representation based models for damage classification.

3.6.1 Dataset Description and Training

We have created a dataset of 135 images having 3000×4000 resolution and annotated these for semantic and instance segmentation using 6 classes: debris, water, building, vegetation, path, and vehicles. Figure 3.13 shows the pixel distribution for each class in the Hurley dataset. The dataset is split into training, testing, and validation with each category having 75%, 15%, and 10% of images, respectively.

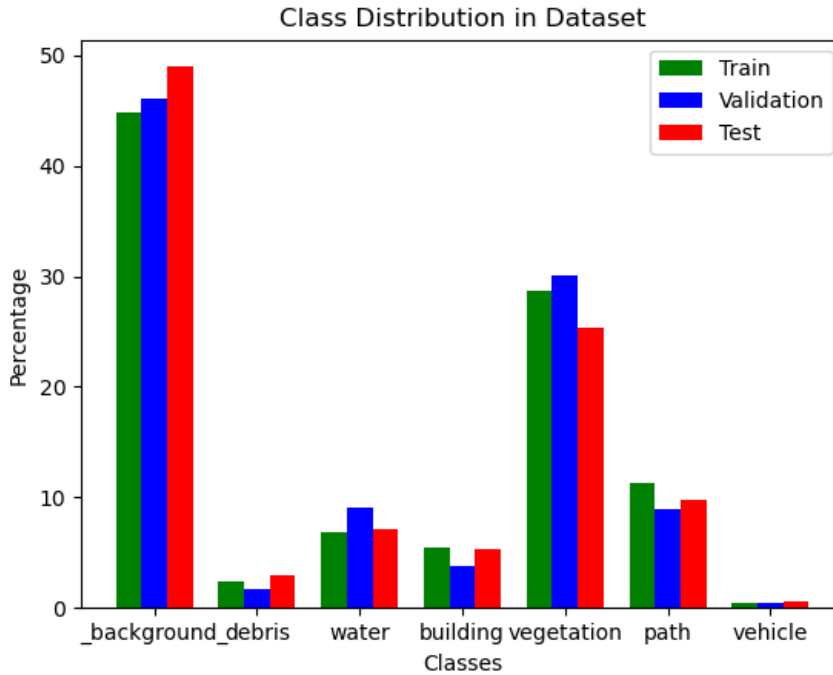


Figure 3.13: Distribution of pixels for each class in the Hurley dataset

While training, the data was augmented with vertical flip, horizontal flip, and random shuffling and trained on image patches with a size of 384×512 pixels. We used focal loss with $\gamma = 4$ as a loss function due to its characteristics for training imbalanced class distributions [76]. The model is trained with a learning rate of 0.001 and a weight decay of 0.0001 using the AdamW (Adam with weight decay) optimizer as it reduces overfitting [77]. We trained the Hurley data using DeepLabV3+, PSPNet, and U-Net architectures with ResNet34 as a backbone.

3.6.2 Segmentation Results

The segmentation results for three networks are compared using the mean Intersection over Union (mIoU) metric. Figure 3.14 shows an example image from our dataset along with our

ground truth labels and the label colormap.

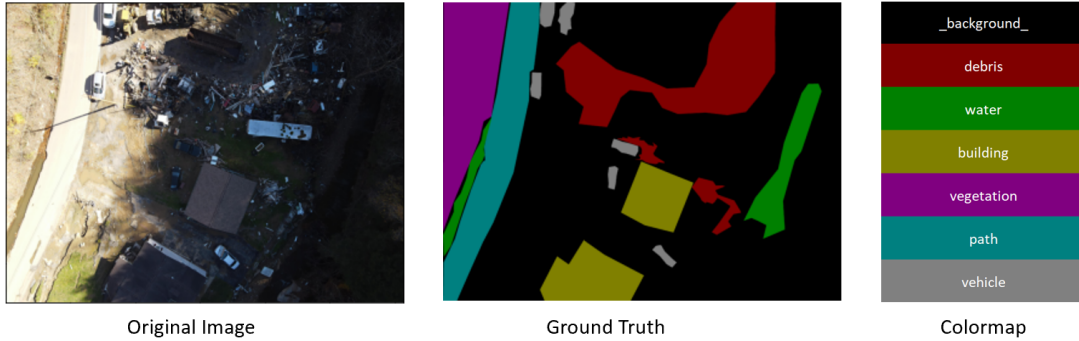


Figure 3.14: Original Image and Ground Truth

From Table 3.4 and Figure 3.15, it is observed that DeepLabV3+ is better at detecting debris and has overall higher mIoU of 19.2% compared to UNet and PSPNet. All models perform well in detecting water, building, vegetation, and path. The vehicle class includes all categories of vehicles, such as construction vehicles, cars, and recreational vehicle (RVs) and represents less than 1% of all pixel values. As a result, these models struggled to categorize this class in some cases. These results show that debris volume can be observed using semantic segmentation techniques and there is room for improvement in existing research on disaster damage analysis. Even though the mIoU score for the debris class is lower than that for the other classes, it gives a good representation of debris distribution after the disaster. We believe that, inherently, debris segmentation is a hard task as debris gets mixed with water, sand, buildings, etc. It becomes more difficult as segmentation networks rely heavily on good manual annotations, which is very time consuming. We will add more images to this dataset in the future which should improve our segmentation results. We will also categorize building damage as per FEMA requirements [20]. This work shows that debris analysis can be helpful for post-disaster SAR missions and restoration as we reduce the search space to specific areas in the environment. The future work will be focused towards improving these

segmentation results and segmenting 3-D point clouds of the Hurley environment.

Table 3.4: Mean IOU results for each class on the Test Set

Network	Debris	Water	Building	vegetation	path	vehicle	mIoU(%)
DeepLabV3+	19.2	48.4	57.11	63.37	46.04	22.9	46.34
PSPNet	13.79	42.50	61.91	58.15	37.71	20.58	41.74
U-Net	16.05	37.78	56.87	58.69	43.24	26.2	43.53

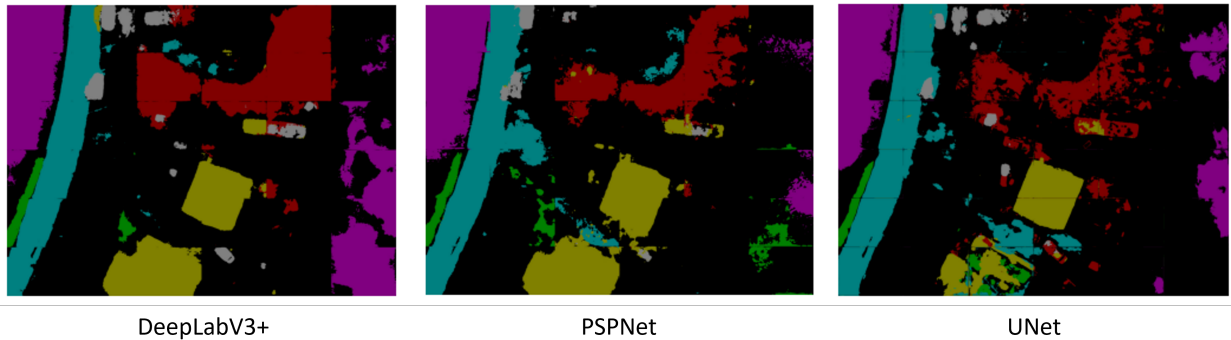


Figure 3.15: Semantic segmentation results comparison of DeepLabV3+, PSPNet and UNet

3.7 Conclusions

The information gained from HEC-RAS flood simulations can be used in multiple different stages of disaster emergency management, including preparedness, response, and recovery. In addition to this, the image segmentation damage analysis is particularly useful for disaster response and recovery efforts. Through measurements acquired after the flood event in Hurley, we were able to verify the accuracy of 2-dimensional HEC-RAS simulations for flood modeling of the water depth. Accurate flood event simulations have many applications for managing this type of natural disaster. When a large rainfall event has been predicted to occur, forecasted precipitation values or weather data from previous events could be used to simulate potential impacts of the flood event. Knowing these potential impacts and flood

water depths can help response crews be prepared for the damage which may occur from this event. Due to a lack of aerial imagery from before the flood in our test case, we used openly available terrain models which were several years out of date. While this proved to be accurate, local communities could potentially improve this accuracy even more by flying drones regularly and keeping up-to-date aerial imagery for terrain modeling. In addition to preparation and response, HEC-RAS flood simulations can be used to inform and improve recovery efforts after the disaster has occurred. For our test area, the new terrain was discovered to be more susceptible to damage if the same rainfall event were to occur again, while progress was being made to restore the roads and homes in the area, debris left in the stream could negatively affect the water flow during future rainfall events. As a result, rebuilding efforts could use the flood simulation information to improve streams and the flow of water through the area in order to mitigate the impacts of any future floods. This enables recovery efforts to also aid in preparation and response efforts for any potential future flood events by creating flood models based on updated terrain information after a disaster. In the future, we plan to incorporate sediment flow into our HEC-RAS flood simulations to more accurately represent the flood event. In addition to this, we plan to test water flow models to calculate input flow hydrographs rather than sourcing this data from the online. This could enable improved predictive modeling before an expected flood event in order to improve response efforts.

The collection of aerial imagery with drones immediately after a natural disaster can greatly assist response efforts in other ways as well. 3D reconstruction software, such as OpenDroneMap, can enable the creation of accurate and detailed models of the damage shortly after a natural disaster occurs. In addition to manually reviewing this imagery for response efforts, semantic segmentation can be performed to analyze and quantify the damage which has occurred, while state-of-the-art flood inundation models still often use bare earth mod-

els with low resolution between 2 and 5 m, improved quality and resolution is needed for more accurate and reliable modeling [48]. The high-resolution imagery acquired from drones can enable detailed property damage and risk values that could not be obtained with other imagery sources, such as satellites. While our debris segmentation models are still a work in progress, we expect accuracy improvement as more training imagery is added. Additional work on our segmentation models will be performed to improve the ability to detect debris as well as using 3-D point clouds of the post-disaster environment to classify damage.

Chapter 4

The Impact of Surface Mining and Mine Reclamation on Surface Runoff and Flood Risk in Appalachia

4.1 Abstract

In the Appalachian area of the United States, significant surface coal mining has altered large areas of the terrain and landscape. These changes have resulted in major impacts on the environment and hydrology of the area. In addition to this, major rainfall and flooding events have continued to become more prevalent due to climate change. This work investigates the impact the terrain disruption due to surface mining has had on surface runoff and flooding. In particular, the focus is on an area of Eastern Kentucky which was severely impacted by floods in July 2022. Through the digitization of historical topographic maps, pre-mining terrain and land cover is compared to the current landscape with respect to surface runoff and flood potential. Additionally, multiple mine reclamation methods were looked at to compare methods for reducing the risk of major flooding in the future after mining has been completed. SWAT simulations showed a significant increase in surface runoff resulted from the coal mining in the area. Mine reclamation methods show the potential to reduce the amount of surface runoff, although not quite to pre-mined levels. HEC-RAS simulations

showed localized increases in flooding resulting from mine lands, while the impacts were less further downstream from the mines. While the flood event looked at in this study would result in major flooding regardless, the coal mining in the area appears to have worsened the flood impacts. Although the impact which surface mining has had on the environment can not be fully reversed, significant improvements can be made to prevent future flooding in these areas.

4.2 Introduction

The Appalachian region is a leading producer of coal in the United States, with major areas of operation in Eastern Kentucky, Southern West Virginia, and Western Virginia. Surface coal mining is common in this area, which involves removing parts or all of mountaintops to expose buried seams of coal and disposing excess overburden and interburden rocks in adjacent valleys. Figure 4.1 shows a representation of the surface coal mining process from the EPA. The former mountain contour is removed to reach the coal seam. Removed rocks are filled into valleys and can flow into nearby streams and rivers as well [43]. Surface coal mining has contributed to the destruction of over 500 mountain tops in Appalachia [71]. According to a 2011 EPA report, surface mining leads to springs and perennial streams being lost permanently, concentrations of major chemical ions downstream, and degraded water quality which can become lethal to organisms [61]. The Surface Mining Control and Reclamation Act of 1977 (SMCRA) requires regrading and re-vegetation once coal removal is complete. The mine is required to be reclaimed to "AOC" or "approximate original contours" unless this requirement has been waived [43].

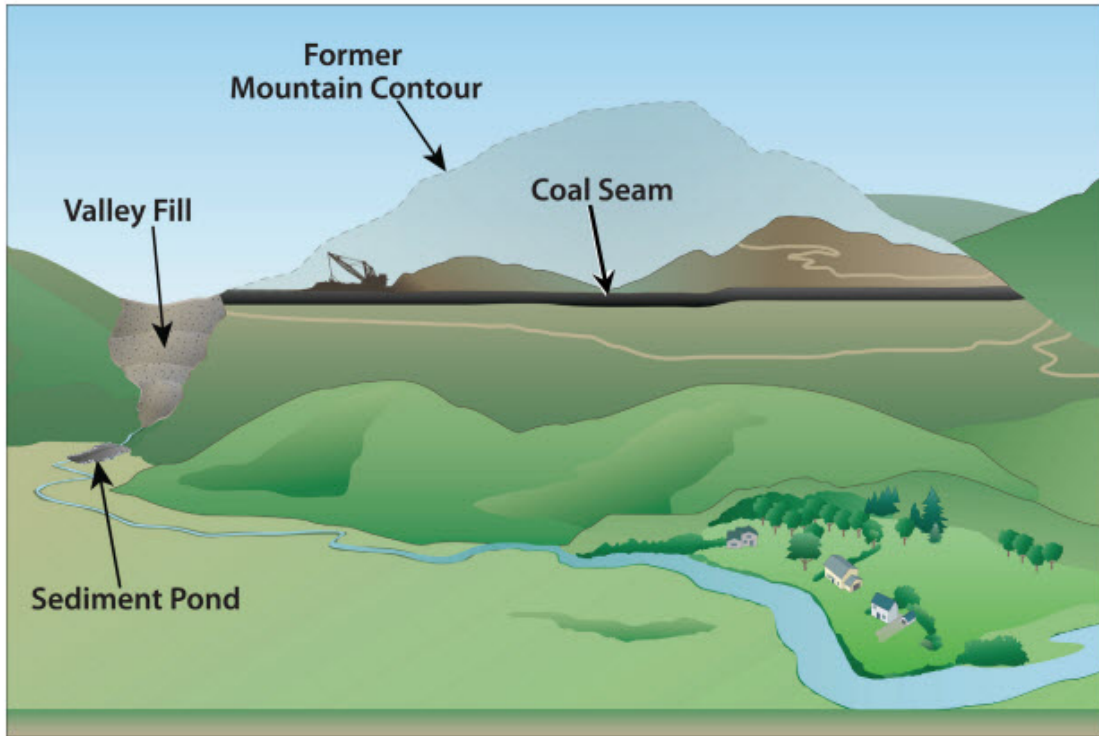


Figure 4.1: A representation of surface coal mining from the EPA. The former mountain contour is removed in order to reach the coal seam, while the excess rocks are disposed of by filling adjacent valleys [43].

Natural disasters have continued to become more prevalent and extreme in recent years, driven by climate change and other factors. Due to the continuing increase in this prevalence of extreme weather events, the impacts from surface mining have continued to become more important. In July 2022, a large flood event occurred in eastern Kentucky. An estimated 14-16 inches of rain fell in a 5-day period. This resulted in almost 9,000 homes in 13 counties being damaged or destroyed and the death of over 40 people [70]. An aerial image of some of the flooding impacts from this event is shown in Figure 4.2.



Figure 4.2: An aerial image of the flash flooding in Eastern Kentucky during the July 2022 event. The flood waters can be seen covering many streets and partial houses. From Leandro Lozada/AFP via Getty Images, published on npr.org [70].

Multiple articles have pointed to the coal mining in this area as a reason for increasing the risk and impacts of the flooding in these areas [68, 79, 85]. One recent paper found the maximum additional water that could have been contributed by surface coal mining to be 28 percent near Jackson, Kentucky and over 50 percent more in areas adjacent to mined lands [67]. While this has been commonly discussed, numerical studies to quantify the impacts have not been as prevalent. As a result, this work aims to quantify the impact which surface coal mining has had on surface runoff and flooding in this area of Eastern Kentucky. SWAT simulations are performed to compare surface runoff for pre-mining conditions, current mined conditions, and multiple reclaimed mine land conditions. After this, HEC-RAS simulations are performed to look at the July 2022 flood event and compare flood depths for pre-mining, current, and reclaimed mine land conditions.

4.3 Materials and Methods

4.3.1 Investigation Area

The investigation area for this study looks at the North Fork of the Kentucky River between Hazard, Kentucky and Jackson, Kentucky. A screenshot of this area from QGIS using Google Maps satellite base map imagery is shown in Figure 4.3. The North Fork of the Kentucky River is drawn in blue on this image to display the river focused on during this investigation. The cities of Hazard and Jackson have been labeled on the map. These cities are significant due to the presence of river monitoring stations, which will be discussed in a later section. The red rectangle represents the mined land which is being looked at for this study. The creation of the coal mines here resulted in the loss of mountaintops and trees from the forested area.

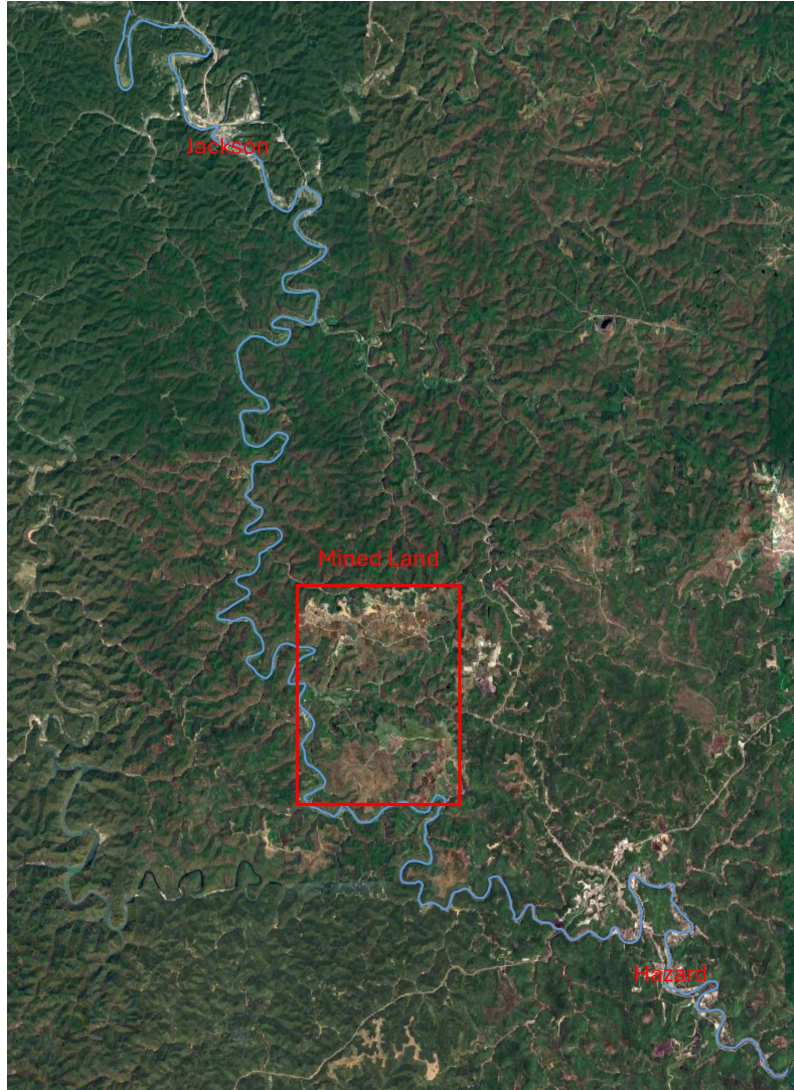


Figure 4.3: A screenshot of the investigation area taken from QGIS with Google Maps base imagery. The cities of Hazard and Jackson are labeled along with the mined land area of interest for this work.

4.3.2 Pre-Mined and Post-Mined Terrain

The state of Kentucky has an Elevation Data and Aerial Photography Program known as KyFromAbove [44]. Elevation data for the state is collected and updated using LiDAR (Light Detection and Ranging) to generate point clouds as well as DEMs (Digital Elevation

Models). DEMs with a resolution of 5 feet are available for the state. For the investigation area, DEMs were available from collections ranging between 2012 and 2017. While these are slightly out of date, they will represent the terrain after mining for this study. An image of the DEM for the investigation area is shown in Figure 4.4.

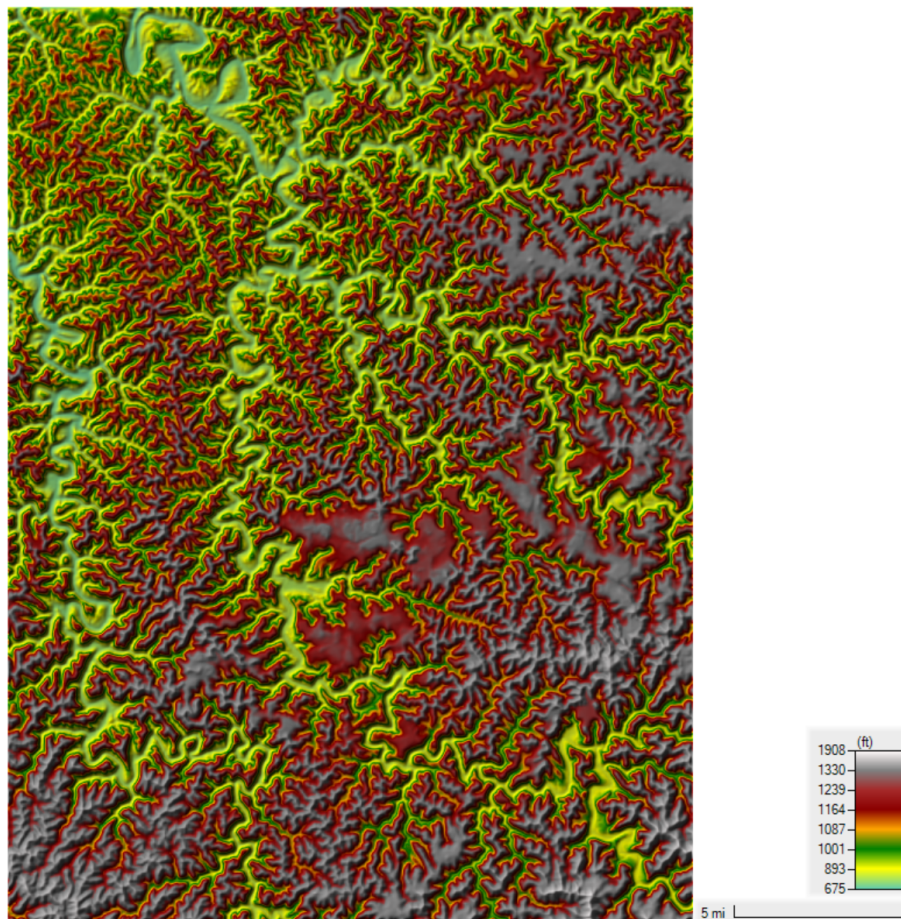


Figure 4.4: The composite DEM created from the data available in the KyFromAbove dataset. The color scale on the right shows the terrain height between 675 and 1908 feet.

In order to determine the terrain from before mining occurred, a historical topographic map from the USGS was used. A topographic map from 1972 from selected due to the map displaying terrain from before mountaintop removal occurred for mining. While older maps are available, many of the older maps have much lower resolution and quality. Figure 4.5

shows a portion of the topographic map from 1972 and another from 2022 in order to show the changes in the terrain.



Figure 4.5: Topographic map comparison for one of the mined areas. The map on the left shows the terrain contours from 1972, before significant mountaintop removal occurred. The map on the right shows the terrain in 2022, after the removal of many mountaintops.

In order to recreate a Digital Elevation Model which represents the terrain from before the mountaintop removal, the 1972 topographical map was used. Figure 4.6 shows the shapefiles created in QGIS corresponding to the contours from the topographical map. These contours represent 40 foot changes in elevation and were used to create a new Digital Elevation Model segment for the mined area.



Figure 4.6: The digitization of the topographic map contours performed in QGIS. The left image shows the contours from the topographic map document. The image on the right shows shapefiles created in QGIS based upon these contours.

After the creation of the new DEM segment representing the mined area, this segment was merged with the other portions of the Digital Elevation Model to produce an approximate representation of the terrain before the mining. Figure 4.7 shows a portion of the DEM with the terrain before and after the mountaintop removal process. Mountain peaks can be seen to have been removed with valleys also being filled. The mined terrain is much more flat compared to the terrain before mining occurred.



Figure 4.7: A comparison of the terrain in a mined area. The image on the left shows the present terrain downloaded from the Kentucky database. The image on the right shows a recreation of the terrain from 1972. The mountaintops and valleys can be distinctly seen compared to the present terrain.

4.3.3 Simulation Input Data

At the south portion of our investigation area, which is the upstream portion, a USGS monitoring location is present in the North Fork of the Kentucky River at the city of Hazard (ID: 03277500). An additional monitoring location is present downstream on the same river at Jackson, Kentucky (ID: 03280000). These two monitoring stations can be used to provide streamflow discharge in cubic feet per second and gauge height of the stream in feet. A map of the two monitoring stations from the USGS website can be seen in Figure 4.8. The streamflow data from Hazard, Kentucky can be used as an input for simulations representing the July 2022 flood event in this area.

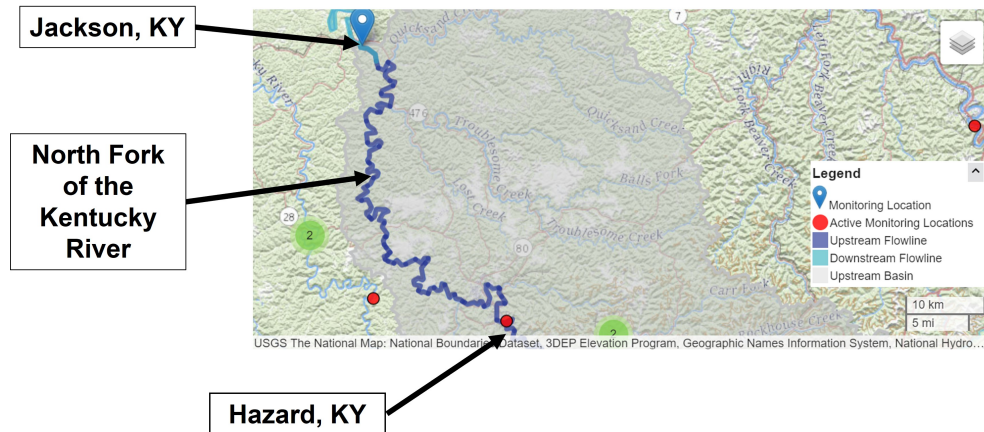


Figure 4.8: The location of the USGS monitoring stations in Hazard, Kentucky and Jackson, Kentucky. This was taken as a screenshot of the image provided by USGS [103].

Precipitation data from the flood event was taken from the NOAA MRMS (Multi-Radar Multi-Sensor) System. A screenshot of rainfall over a 72-hour period for this area is shown in Figure 4.9. This figure shows portions of the investigation area which received over 12 inches of rainfall in a 72 hour period.

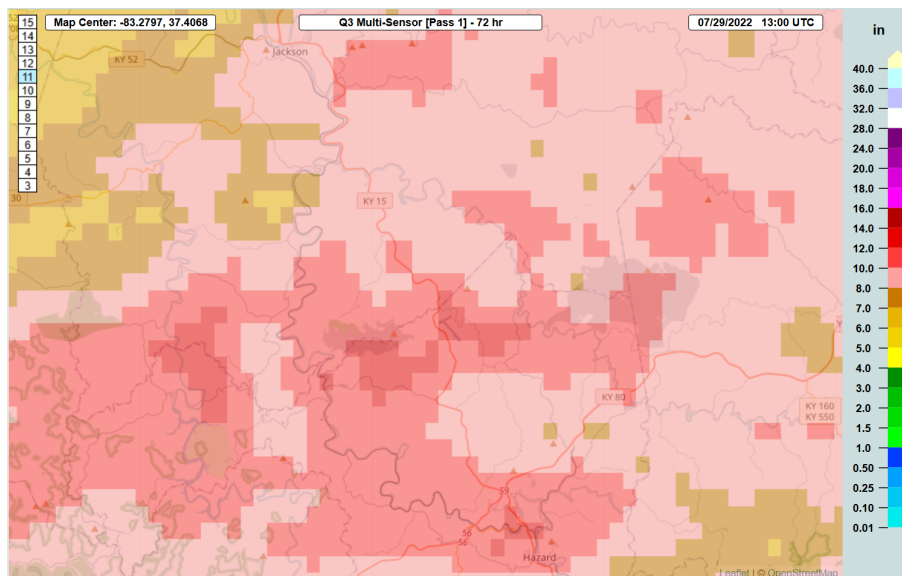


Figure 4.9: The precipitation from the NOAA MRMS system measured over a 72 hour period for the investigation area between Hazard and Jackson. Peak areas received over 12 inches of rainfall during this 72 hour window.

4.4 Surface Runoff Simulations

In order to determine the amount of surface runoff in our investigation area and compare the effects of mine land, various SWAT (Soil and Water Assessment Tool) simulations were performed. For these simulations, the area used was from Hazard, Kentucky up to just north of the mined areas being examined.

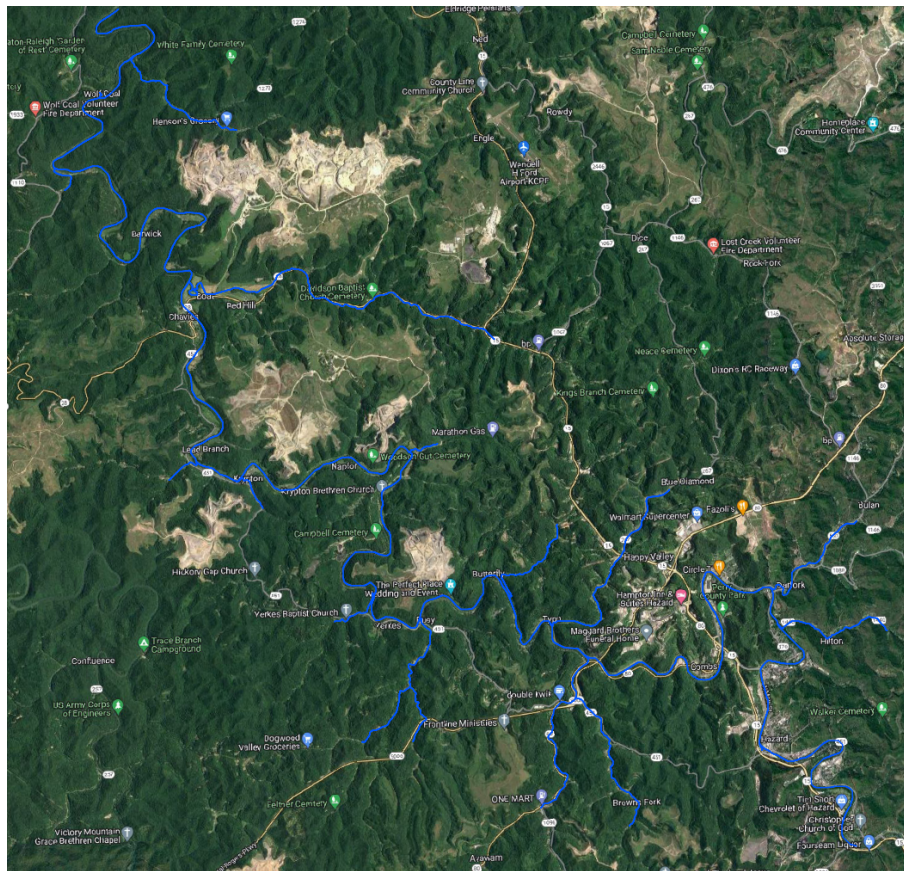


Figure 4.10: The study area used for the SWAT simulations. The North Fork of the Kentucky River and connected streams are shown by the blue lines in the image. The mined areas can be seen nearby portions of the river.

4.4.1 Simulation Parameters

The land cover data was taken from the 2021 USGS National Land Cover Database (NLCD). The base land cover data for the investigation area is shown in Figure 4.11. The majority of the investigation area is covered in deciduous forest, with the mined areas and developed areas also covering portions.

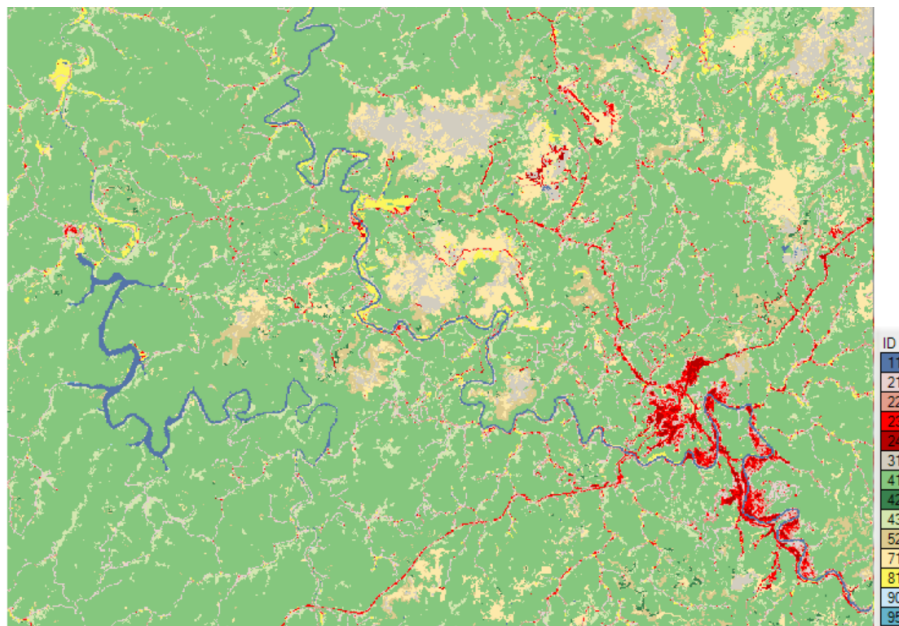


Figure 4.11: The land cover of the area acquired from the 2021 NLCD. The ID on the right shows the colors corresponding to the land cover types.

The soil data for this area was acquired from the Soil Survey Geographic Database (SSURGO). The data is available to download through the USGS NRCS (Natural Resources Conservation Service) Web Soil Survey [99]. The corresponding SWAT US SSURGO Soils Database was used along with the data during the SWAT simulations. [101]. The soil map for the study area is shown in Figure 4.12 along with the corresponding SWAT SSURGO labels.

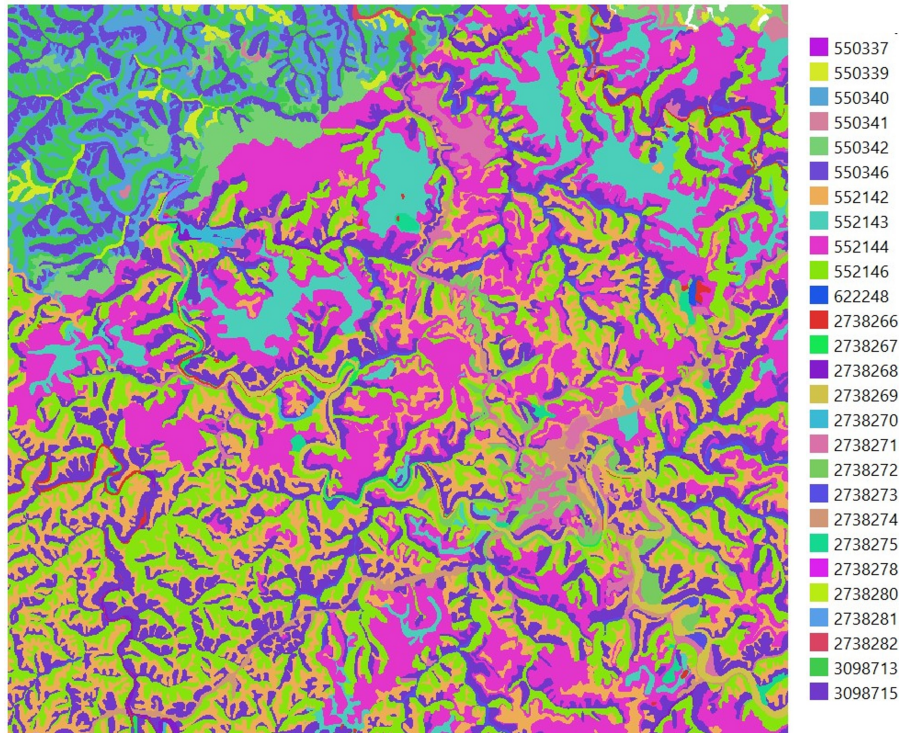


Figure 4.12: The soil types of the area acquired from the SSURGO Database. The ID on the right shows the colors corresponding to the soil types.

SWAT Simulations were performed to examine and compare the surface runoff for the investigation area. Six different combinations of terrain and land cover were examined in this study. The first combination uses the current terrain of the mine along with the barren land class for the land cover of the mine. The second combination uses the pre-mined terrain along with Deciduous Forest land cover of the terrain to represent the forest and terrain which existed before the mine was created. The third combination looks at a theoretical situation where the pre-mined mountain terrain had the same land cover as the mine. This was used to see the impact of only changing the terrain instead of both the terrain and land cover. The final three combinations look at different mine land reclamation methods. These each use the current terrain of the mine, but involve changing the land cover to represent returning vegetation to the previously barren land. The three land cover types examined are

deciduous forest, grassland, and shrubland.

Due to large gaps in the long-term data for the area, these SWAT simulation scenarios used simulated weather data from within SWAT. By using simulated data, we see the impact of these terrain and land cover combinations on surface runoff during average weather circumstances rather than extreme flood scenarios. The same input weather data was used for each of the six different simulation scenarios. The rainfall for the test area was an average of 1137 mm per year over the simulation period.

While the soil data was available for the current mined land, historical data from before the mining is much more difficult to find. As a result of this, the soil map for pre-mined forest area was adjusted to reflect the soil of nearby mountains rather than the soil from the mined terrain. The Fairpoint series soil in the mined area was replaced with a combination of Shelocta and Matewan series soils to match with the soils from nearby forested mountains. For the reclaimed mine land simulations, soil maps similar to that of the pre-mined terrain was used to determine the impacts of a full reclamation effort which includes replacing soil similar to what existed before the mining occurred.

The watershed in SWAT for this study covers an area of 3347.7 square kilometers. The mined land area of interest within the watershed covers an area of about 50 square kilometers. The watershed in SWAT was delineated into 35 subbasins for the analysis. Figure 4.13 shows the SWAT subbasins overlaid on the Digital Elevation Model for the investigation area.

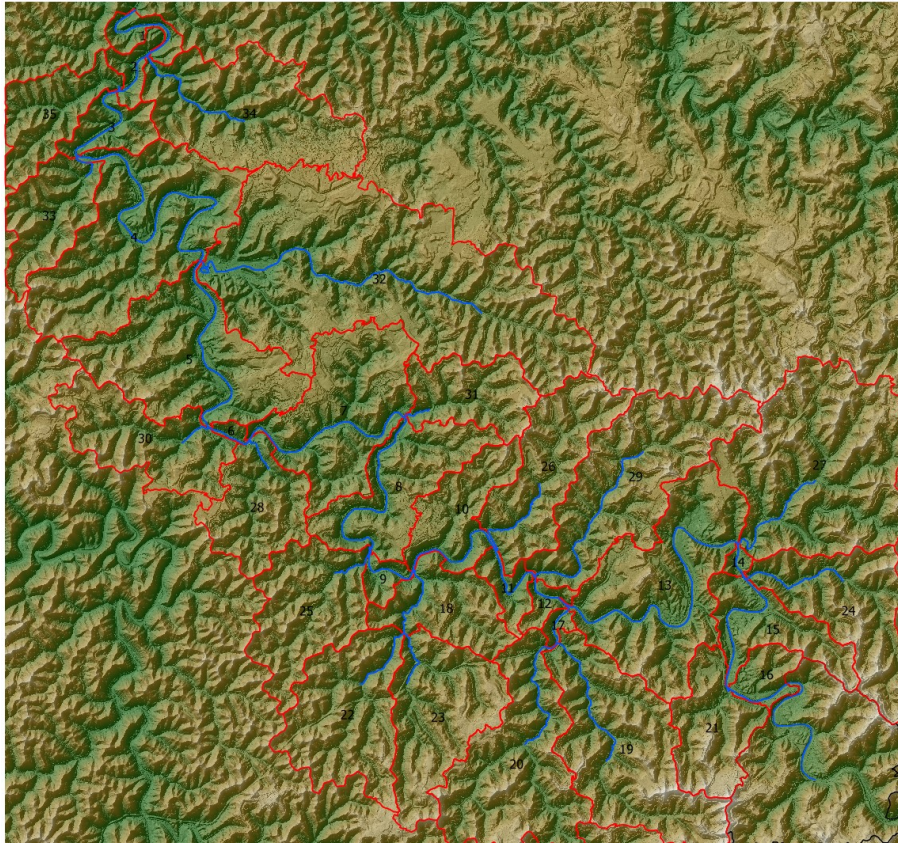


Figure 4.13: The watershed delineation in SWAT. The blue lines represent the stream reaches and the red outlines represent the subbasins.

4.4.2 Simulation Results

The SWAT simulations were performed over a 21-year time period with the first 5 years being used for warmup. The results from the SWAT simulations are summarized in Table 4.1. The barren land cover scenarios had the highest runoff, with the values being the same for both the mined and pre-mine terrain. The pre-mined terrain with forest land cover produced 35.8 percent less runoff than the barren land cover of the mine. This represents a 55.8 percent increase in runoff due to the mining in this area. The three reclamation methods each showed a noticeable decrease in surface runoff compared to the mined terrain. These resulted in 35.8

percent less runoff with forest land cover, 33.5 percent less runoff with grassland land cover, and 30.8 percent less runoff for shrub land cover. These results show promising potential for mine land reclamation to reduce surface runoff. These reclamation scenarios represent ideal situations, which may not be entirely realistic. Returning forests to the land would likely not be feasible due to the time and effort required. Reclamation using grassland and shrub land are much more realistic than forest. The reclamation scenarios for the simulation used the return of soil similar to the original pre-mined soil, which is an ideal scenario. Adding additional soil during the reclamation process similar to the pre-mined soil should help, but would likely not reach pre-mined runoff levels.

Table 4.1: The average surface runoff per year resulting from the SWAT simulations for each of the six terrain and land cover combinations.

Terrain	Land Cover	Surface Runoff (mm)
Mined	Barren Land	83.22
Pre-mined	Deciduous Forest	53.43
Pre-mined	Barren Land	83.22
Mined	Deciduous Forest	53.46
Mined	Grassland	55.35
Mined	Shrub	57.62

4.5 Flood Depth Simulations

In order to simulate the flood event which occurred in the investigation area in July 2022, HEC-RAS (Hydrologic Engineering Center’s River Analysis System) was used. HEC-RAS is an open-source software which is available through the US Army Corps of Engineers. HEC-RAS allows users to perform one-dimensional steady flow, one and two-dimensional unsteady flow calculations, sediment transport and mobile bed computations, and water temperature and water quality modeling [28].

4.5.1 Simulation Inputs and Parameters

Two-Dimensional unsteady flow modeling was performed in HEC-RAS in order to model and simulate the flood event from 2022. A larger area than the previous SWAT simulations was used in order to capture the USGS monitoring locations in both Hazard and Jackson. This enabled the flow measurements at Hazard to be used as an input to the river along with water height values at Jackson for determining the accuracy of the simulations. For the 2D flow area mesh, point spacing of 100 ft by 100 ft was used with breaklines enforced along the center and banks of the North Fork of the Kentucky River. This resulted in a mesh with 890,698 cells for the simulation area. Different computation intervals were tested in order ensure the numerical analysis was stable. The baseline computation interval for the simulation was set to 15 minutes for all of the simulations. To further improve the stability of the model, the variable time step options was used in order to set a maximum Courant number for the simulation. While a stable and accurate solution could be achieved with a Courant number as high as 5, the maximum value should be set closer to 1 when modeling more rapid changes of depth and velocity. Due to the rapid nature of this flood event, the maximum Courant number was set to 1 for the simulations.

From the flood event which occurred in July 2022, the rainfall data was used from the NOAA MRMS for the period between July 25, 2022 at 12:00 AM and July 31, 2022 at 11:00 PM. The gridded precipitation data for the simulation area was used as the Meteorological Precipitation data of the HEC-RAS unsteady flow data input.

The inlet boundary condition was set to the location of the USGS flow monitoring station at Hazard, Kentucky. This boundary condition used a flow hydrograph with data collected at this station between July 25 and July 31. The streamflow data collected at this flow station is shown in Figure 4.14. The flow station recorded a peak discharge of almost 20,000

cubic feet per second during this flood event. At the downstream outlet boundary condition, Normal Depth was used in HEC-RAS.

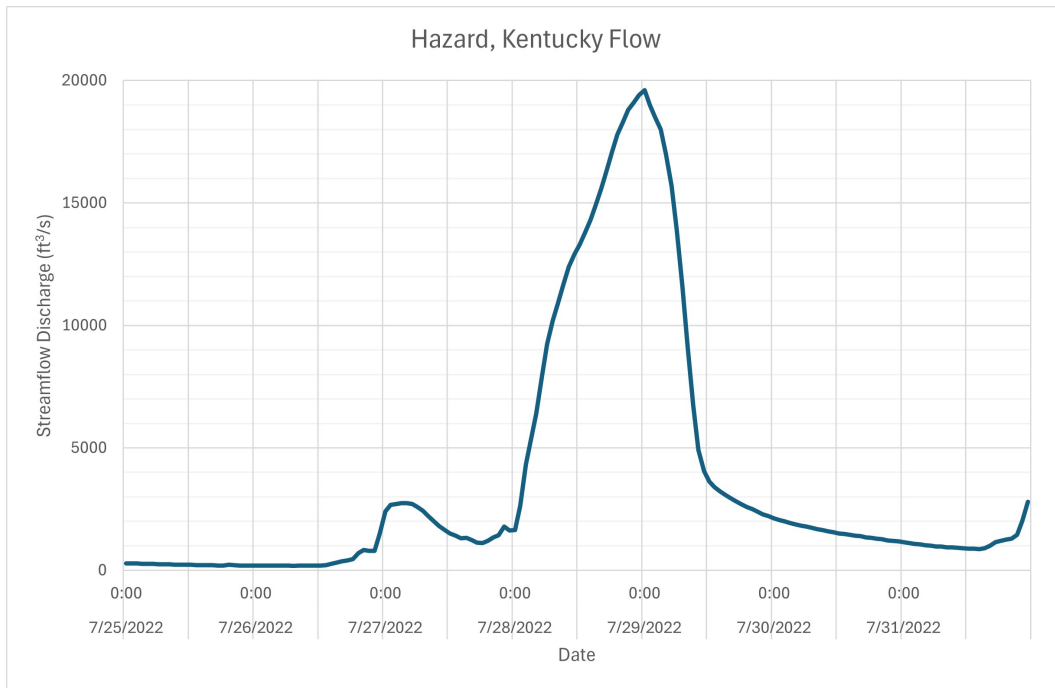


Figure 4.14: The streamflow discharge measured at the monitoring station in Hazard, Kentucky between July 25 and July 31 2022.

Land Cover data was retrieved from the 2021 USGS National Land Cover Database. The 2021 NLCD was used as the default land cover and the mined portions were adjusted as necessary for each of the subsequent scenarios. The Manning's N values and Percent Impervious values for each of the land cover classes were initially set based upon the recommendations and example values from the HEC-RAS documentation [50]. The values which were used in the HEC-RAS simulations for each land cover class is summarized in Table 4.2.

Table 4.2: The Manning’s N and Percent Impervious values used for each of the land cover types in the HEC-RAS simulations. The NLCD ID numbers and class names are included for each.

NLCD ID	Class Name	Manning’s N	Percent Impervious
0	No Data	0.035	0
11	Open Water	0.035	100
21	Developed, Open Space	0.035	10
22	Developed, Low Intensity	0.08	35
23	Developed, Medium Intensity	0.12	65
24	Developed, High Intensity	0.15	90
31	Barren Land, Rock-Sand-Clay	0.03	0
41	Deciduous Forest	0.10	0
42	Evergreen Forest	0.15	0
43	Mixed Forest	0.12	0
52	Shrub-Scrub	0.08	0
71	Grassland-Herbaceous	0.04	0
81	Pasture-Hay	0.045	0
90	Woody Wetlands	0.08	50
95	Emergent Herbaceous Wetlands	0.06	75

An initial simulation of the flood event was performed with terrain and land cover matching as close as possible to the time of the flood event. This used the terrain data from the Kentucky LiDAR database along with the mined land cover remaining as-is. The simulation resulted in a volume accounting error of 0.176 percent, which is very low and good sign of model stability. In order to determine the accuracy of the simulation, the water depth measurement from the simulation was compared to the recorded water height data from the

USGS monitoring station at Jackson, Kentucky. At the monitoring station, the peak water depth was measured to be 43.47 feet. The water depth from the HEC-RAS simulation at the same location was found to only be 37.12 feet, which is 14.6 percent less than the station measurements. While this is a noticeable difference, it is extremely difficult to determine the main cause of this. Many factors likely contributed to the difference, including terrain models which were between 5 and 10 years out of date, any possible errors in the streamflow and precipitation data, and sediment transport not being included in the study. Errors or uncertainty within the input precipitation data would result in localized variations in the model based upon the gridded locations. In order to examine the sensitivity of the model to the land cover Manning's N values, the maximum and minimum values of the recommended ranges were used in addition to the final values from Table 4.2. The variation of the Manning's N values resulted in water depth values at Jackson, Kentucky ranging between 35.23 feet and 38.56 feet. There is some uncertainty with the water depth values based upon these surface roughness parameters, but the final values selected for the simulations represent results near the center of this range. Although the initial simulation was under predicting the water depth, the results were reasonable enough to continue with our investigation. All of the additional simulations are being performed with the same simulation parameters while only varying the terrain and land cover. As a result, while the water depths may be lower than measured values, this offset can be expected to be consistent across all simulations.

The same six terrain and land cover combinations from the SWAT simulations were used for HEC-RAS as well. This includes the current mined terrain with barren land cover, pre-mined terrain with deciduous forest as well as barren land covers, and mined terrain with three reclamation land covers of deciduous forest, grassland, and shrubland. These six scenarios were used to determine the flood water depths at four different locations along the stream path near and past the mined area. Three of the measurement locations near the

mines are displayed in Figure 4.15. These locations were plotted on a Google Maps base map in QGIS. The North Fork of the Kentucky River is shown in light blue and flows northward around the two major mined areas in the image. The first measurement location is directly west of one portion of mine land. The second measurement location is directly between the two areas of mine land and the third measurement location is at a portion of the river north of the mined areas. These were selected to allow us to examine the localized effects of the terrain and land cover around different portions of the mines.

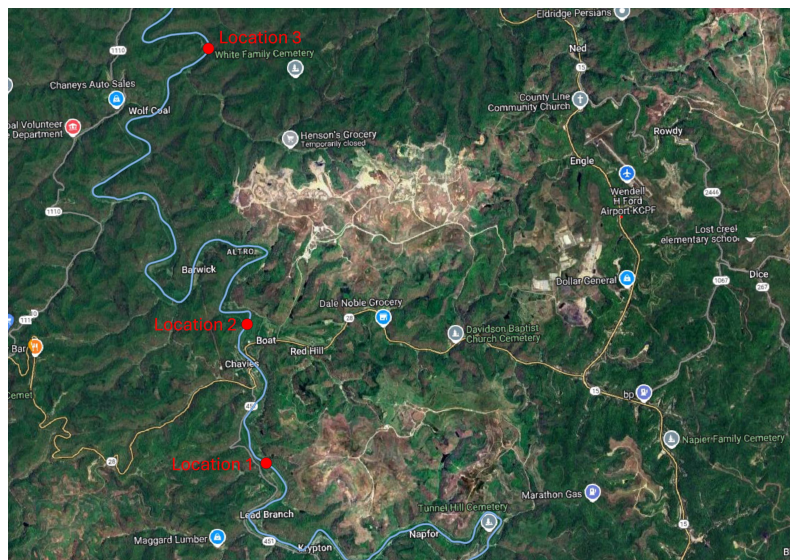


Figure 4.15: The location of three measurements used for comparison for the HEC-RAS simulation results. The locations represent the stream nearby, between, and just downstream of the mined areas of interest.

The fourth measurement location is at the USGS monitoring station location in Jackson, Kentucky. This location allows for a comparison with recorded water depths from the station and to determine the impacts of the mines to a portion of the river much further downstream from the mines. The location of this monitoring station relative to the other three measurement locations is shown in Figure 4.16. In addition, the monitoring station located in Hazard, Kentucky is included as well.

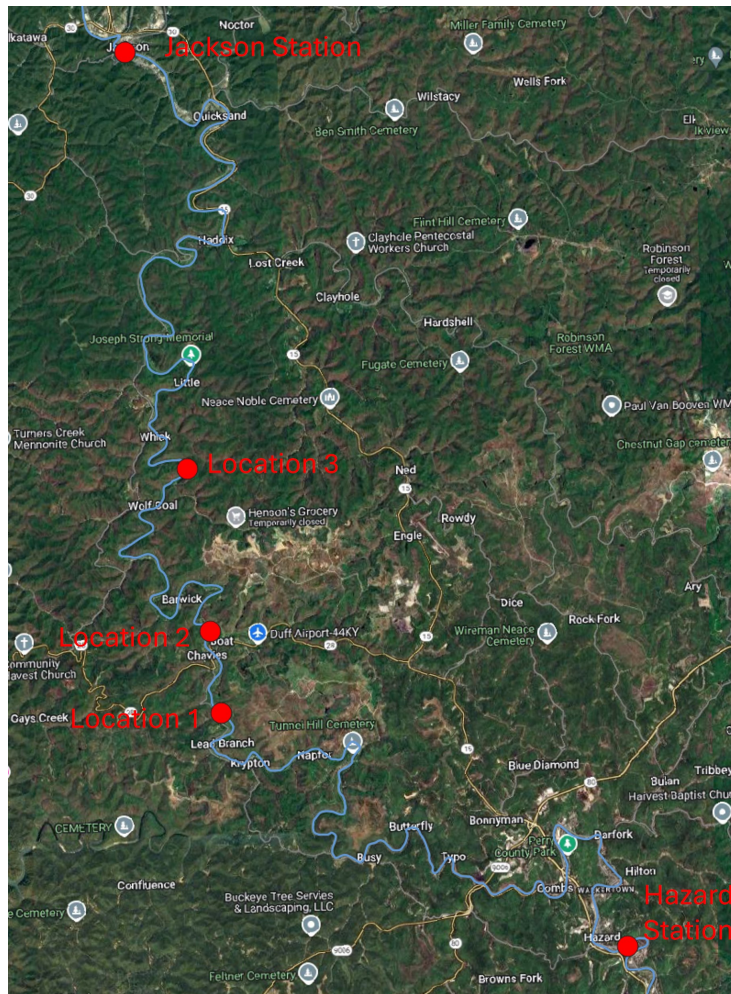


Figure 4.16: The full investigation area showing the three locations from Figure 4.15 along with the locations of the monitoring stations in Hazard and Jackson.

4.5.2 Simulation Results

The results of the simulations for each of the 6 combinations are summarized in Table 4.3. The flood depth measurement results for each of the four locations is included for all simulation combinations. The largest differences in flood depth were seen at Location 2 for these scenarios. The pre-mined forested terrain resulted in the lowest flood depths across all four of the locations. The largest difference in the flood depth was seen in close proximity

to the mined area and the difference trailed off as the distance from the mines increased. Compared to the pre-mined terrain with forest land cover, the mined terrain showed an increase of 5.2 percent at location 1, 6.3 percent at location 2, 4.5 percent at location 3, and 4.2 percent at the station in Jackson. The pre-mine terrain with barren land cover showed almost no difference in flood depth compared to the mined terrain. The three reclamation methods reduced the flood depths by a very small amount at most of the locations compared to the mined terrain, with the largest being a 2.2 percent reduction at location 2 for the forest land cover. At the monitoring location in Jackson, the three reclamation methods resulted in almost no change in flood depths, with the largest being a decrease of 0.57 percent for the shrub land cover.

Table 4.3: The flood depths at four different locations for each of the six HEC-RAS simulations.

Terrain	Land Cover	Location 1 Depth (ft)	Location 2 Depth (ft)	Location 3 Depth (ft)	Jackson Depth (ft)
Mined	Barren Land	34.16	36.03	33.08	37.12
Pre-mined	Deciduous Forest	32.47	33.90	31.65	35.61
Pre-mined	Barren Land	33.67	36.25	33.01	37.12
Mined	Deciduous Forest	33.67	35.22	33.05	37.07
Mined	Grassland	33.92	36.22	32.86	37.14
Mined	Shrub	33.55	35.42	33.06	36.91

In order to see the variation of the water depth over time for the simulations, the results can be plotted. The plot in Figure 4.17 shows the simulated water depth over time at measurement location 2 for three of the scenarios. The three scenarios shown are mined terrain with barren land cover, pre-mined terrain with forest land cover, and mined terrain with forest land cover. The plots show a more complete view of the water depth compared to only the peak water depth. Based on this, the pre-mined forest scenario can be seen to reach a lower peak value around the same time as the mined scenario while also receding

to lower values at a quicker rate. The reclaimed forest scenario reaches a slightly lower peak water depth value than the mined scenario, but follows a similar path while receding. Based on the plot, the reclaimed mine land with forest land cover shows a very similar water depth profile despite the slightly lower peak value. This water depth plot highlights an even more noticeable difference between the pre-mining and mined scenarios with respect to the amount of water depth as well as the duration of these peak water depth values.

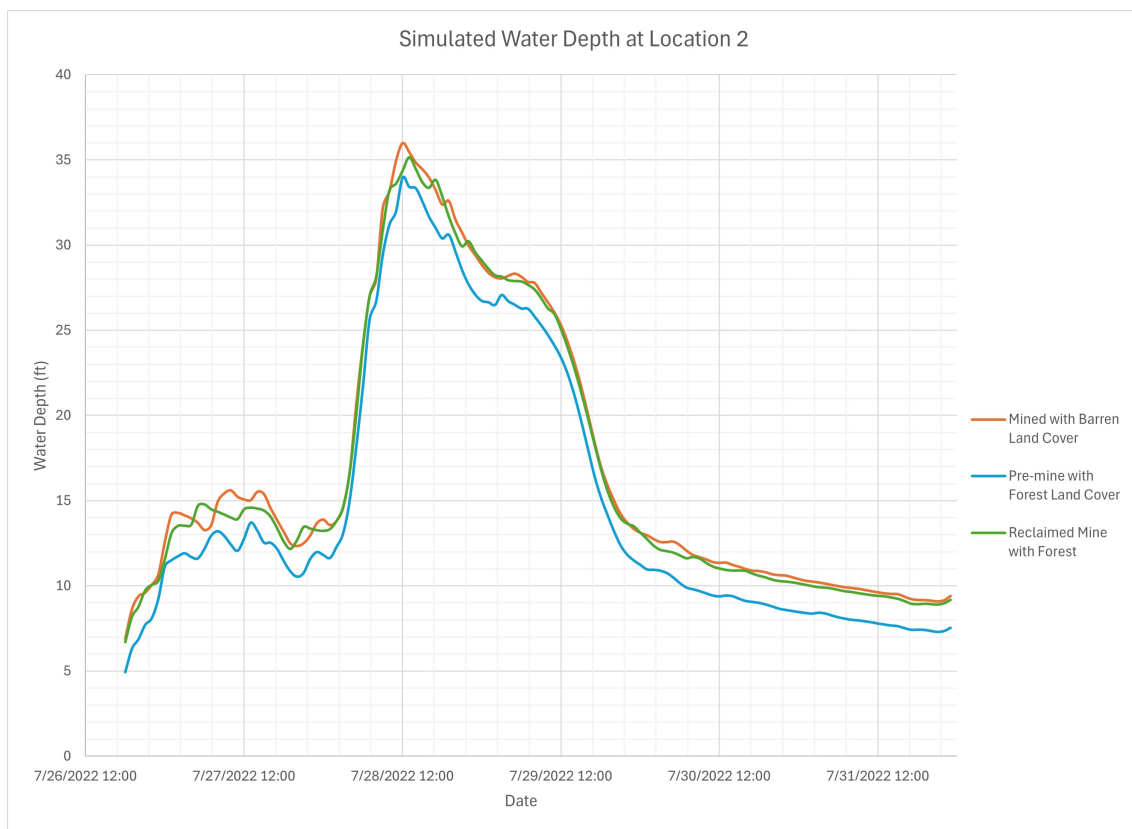


Figure 4.17: A comparison of the HEC-RAS water depth results over time for three of the simulations. These include the current mine land with barren land cover, the pre-mined terrain with forest land cover, and the reclaimed scenario with forest land cover.

Figure 4.18 shows a comparison between the flood depths of a mined area and the pre-mined area with forest land cover. The pre-mined terrain shows more confined water flow through the valleys of the mountains, while the mined terrain shows more wide-spread standing water

over the area. The mined terrain also shows higher peak water depths with the water not having natural paths to flow.

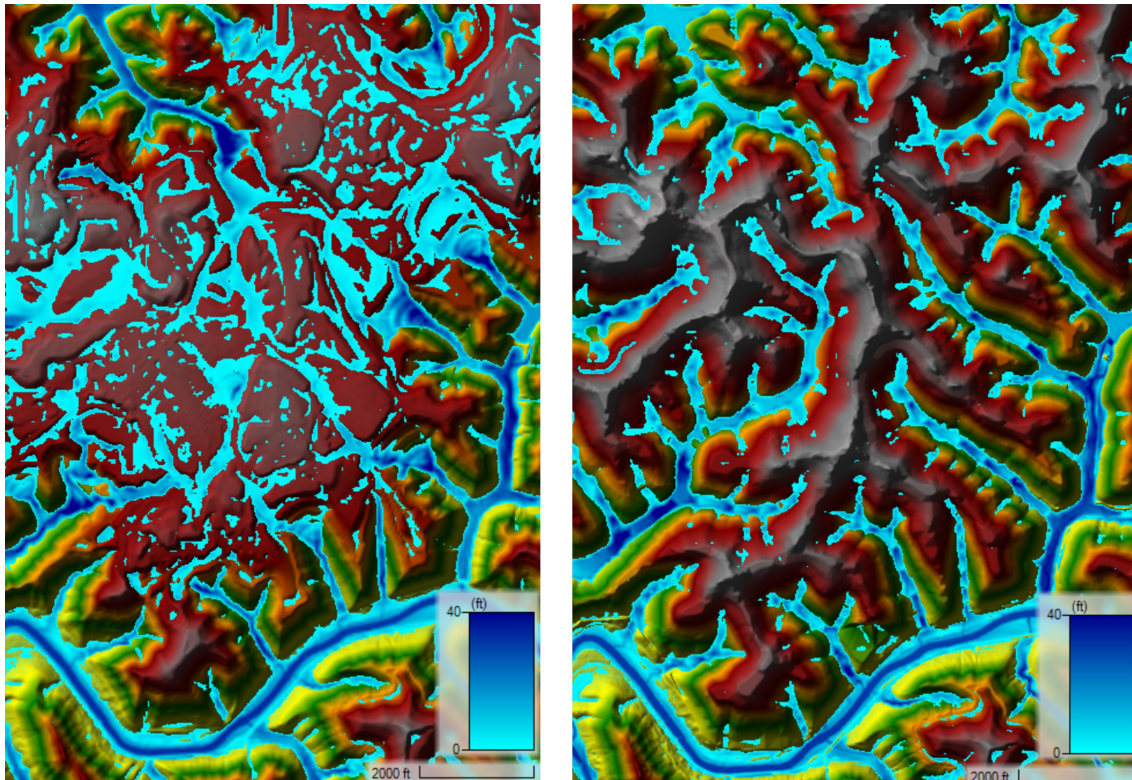


Figure 4.18: A comparison of the HEC-RAS water depth results from two the simulations. The left image shows results for an area of mined terrain with barren land cover. The image on the right shows the corresponding area of pre-mine terrain with deciduous forest land cover.

4.6 Discussion and Conclusions

Based upon both the SWAT and HEC-RAS simulations, the change in terrain from forest covered mountains to mine land has resulted in noticeable increases in surface runoff as well as flood depths for a major flood event. The surface runoff showed large differences due to the changes in land cover and soil rather than due to changes in terrain only. As a result of this, ideal reclamation methods show promise to reduce the amount of surface

runoff without the need to restore the previous mountaintops. While the ideal scenario of returning the pre-mined soil type and land cover was able to reduce surface runoff close to pre-mined value, this is unfortunately not realistic. Despite this, the growth of grassland or shrubland show promise to reduce the surface runoff compared to the barren mine land. It would likely be very important to replace the soil to some extent, although a full return to pre-mined scenario is impossible.

The impacts of the mined terrain to flooding and runoff appear to be greater in localized areas around the mines compared to further downstream from the event. Due to this, it would be reasonable to assume the impact could compound if there are many additional mined areas in close proximity. While the impacts appear to diminish once a far enough distance downstream has been reached, additional mined areas before such a distance would likely see the impacts of upstream mined areas as well. The most heavily mined portions of Appalachia are likely to see even larger impacts due to the greater amounts of mined areas.

Unfortunately, this analysis has suggested that reclamation techniques for the mined land are unlikely to completely reverse the impact of the surface mining. Despite this, some improvements do seem possible by reclamation. For the many communities in this area and other areas nearby, it is very important to attempt reclamation to any level possible in an effort to reduce the risk of significant flooding.

Chapter 5

Combining Flood Risk and Property Value to Estimate Loss and Damage Risk

In order to demonstrate flood risk to property for estimating loss and damage risk, a section of Hurley, Virginia was selected. An orthophoto from collected drone imagery is shown overlaid on a Google Maps base map in Figure 5.1.



Figure 5.1: An orthophoto created from the drone imagery captured at Hurley, Virginia.

For this portion of Hurley, the previously discussed aerial building segmentation method from

Chapter 2 can be used to find the size and location of property. The segmenting building results can be converted to polygons and shown with the orthophoto image. The building polygons were overlaid onto the orthophoto from Figure 5.1 using QGIS in order to produce the image in Figure 5.2. The building polygons allow the amount and size of the buildings to be easily calculated and seen.



Figure 5.2: Detected building polygons were overlaid onto the orthophoto in Hurley.

The flood modeling results for this area of Hurley discussed in Chapter 3 can be exported from HEC-RAS to be included in this visualization. The maximum flood water depth results were exported from HEC-RAS and imported into QGIS with the building polygons and orthophoto to produce Figure 5.3. In this image, the maximum value of the color scale was selected as 4 meters with all values over this being also shown in red. This maximum was selected because more than the entire first floor of buildings would be underwater at this depth. The building heights in this section, while not shown in the image, were mostly between 4 and 6 meters. As a result, some buildings would be completely underwater with flood depths over 4 meters.

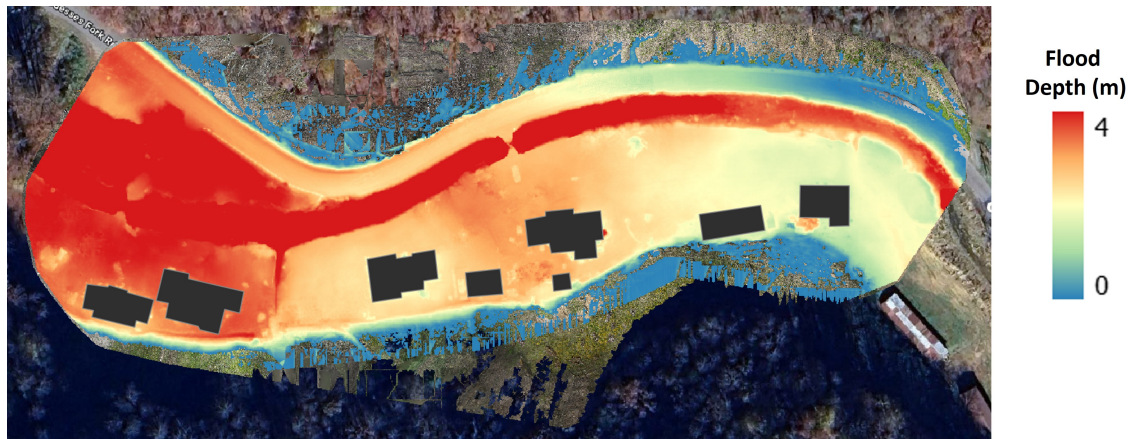


Figure 5.3: Flood water depths displayed in QGIS with the orthophoto and detected buildings for a section of Hurley, Virginia.

The flood depth map can be used to estimate which of the buildings are likely to be destroyed or damaged from a flood event. The estimated properties values of these buildings could then be used to create a comprehensive loss estimate for this specific community from a flood event. In lower resource communities, the building property values could be estimated based upon the calculated size of the buildings from the segmentation results. In many areas of the United States, the property values can be easily accessed through online databases. On a community basis, regularly collected drone imagery can enable up-to-date and extremely accurate flood damage risk. This is not currently available in many areas, especially recent or high-resolution data. As a result, available risk maps are based upon low quality map data and result in low-resolution and inaccurate mapping. This flood risk and damage estimation mapping method presents improvement to the current, state-of-the-art methods which are available and in practice. This flood damage risk information has many uses, including preparing for potential flood events, rebuilding areas after a flood event, and attempting to reduce or mitigate the damage risk.

Chapter 6

Summary and Conclusions

The three articles in this dissertation have presented a methodology for aerial-based flood risk assessment, management, and restoration. Using machine learning approaches on aerial imagery, the size and value of property can be estimated and tracked for any communities. While this is especially useful in the case of low-resource communities, it has applications anywhere. By combining this with flood analysis, we can gain a greater understanding of the areas and property at risk due to flooding events.

The work began by presenting a concept of simplified data collection, 3D cadastre modeling, and natural disaster risk assessment through the use of low-cost drones and adapted open-source software. Collected aerial imagery can be used to produce 3D cadastre models in order to contextualize and quantify potential natural disaster risk to infrastructure and property. By using machine learning semantic segmentation methods, the size and shapes of buildings can be determined and used to provide estimates of the value. The addition of flood risk data enables a comprehensive view of the possible damage and loss from a flooding event.

For a flood event in 2021, an area in Hurley, Virginia was investigated. HEC-RAS was used to simulate the flood event using state digital elevation models and recorded weather conditions. Drone imagery captured after the flood event were used to produce 3D models of the terrain after the flood event. These updated models were used in additional HEC-RAS simulations to find the potential flooding for a future event of the same magnitude would likely be significantly worse. In Hurley, Virginia, combining cadastral information with the

updated flood models can allow us to gain an understanding of the extent of future flood risk due to terrain changes from the 2021 flood event. This should also be used to guide restoration of the area and the streams. If the water flow through this area is left in a disrupted state, the risk for additional flooding and property loss can continue to grow.

An area of Kentucky with significant coal mining was examined to determine the impacts of mined terrain to flooding and surface runoff. Based upon both the SWAT and HEC-RAS simulations, the change in land cover and terrain from forest covered mountains to mine land has resulted in noticeable increases in surface runoff as well as flood depths for a major flood event. The impacts of the mined terrain to flooding and runoff appear to be greater in localized areas around the mines compared to further downstream from the event. Ideal mine land reclamation methods show promise to reduce the amount of surface runoff without the need to restore the previous mountaintops. Unfortunately, this analysis has suggested that reclamation techniques for the mined land are unlikely to completely reverse the impact of the surface mining. In Kentucky, the cadastral information can be combined with flood modeling in order to assess the properties at risk around these heavily mined areas. The information from the study on the mined area can be especially useful for the local areas as they attempt to restore the mine land through reclamation. A combination of the flood simulations and cadastral information enables a more complete view of possible methods to reduce amount and value of property at risk due to flooding in this area. While the event in 2022 was so extreme that significant damage was likely unavoidable, this does not diminish the need for taking action to reduce future risk of damage and property loss.

The combination of high-resolution aerial data for 3D cadastre modeling and corresponding flood risk modeling enables the creation of community-based damage and loss estimates which are currently either unavailable or inaccurate. The tools currently available, such as FEMA's Hazus use large-scale data which leads to low-resolution and often inaccurate risk

assessments. The methods presented in this work improve upon the current state-of-the-art and fill in gaps for the coarse data tools which are available. High-resolution community-based modeling produces improved, up-to-date, and accurate flood risk assessments at the property level for any communities. As a result, the methods presented in this work overcome the shortcomings of the currently available methods to produce accurate and comprehensive flooding risk and damage estimates at the property and community level.

Bibliography

- [1] Hec-ras features. <https://www.hec.usace.army.mil/software/hec-ras/features.aspx>.
- [2] Gis and mapping services. montgomery county, va. <https://montva.com/departments/planning-gis-intro/gis-and-mapping-services>.
- [3] National land cover database class legend and description. <https://www.mrlc.gov/data/legends/national-land-cover-database-class-legend-and-description>.
- [4] Camera module v2. <https://www.raspberrypi.org/products/camera-module-v2/>.
- [5] Pytorch. <https://github.com/pytorch/pytorch>.
- [6] Model stability. hec-ras user's manual. <https://www.hec.usace.army.mil/confluence/rasdocs/rasum/6.0/performing-a-1d-unsteady-flow-analysis/model-accuracy-stability-and-sensitivity/model-stability>.
- [7] Swat: Soil and water assessment tool. <https://swat.tamu.edu/>, .
- [8] Soil and water assessment tool. usda climate hubs. <https://www.climatehubs.usda.gov/hubs/international/tools/soil-and-water-assessment-tool>, .
- [9] Tensorflow. <https://github.com/tensorflow/tensorflow>.
- [10] The human cost of weather related disasters (1995-2015). https://www.unisdr.org/2015/docs/climatechange/COP21_WeatherDisastersReport_2015_FINAL.pdf, 2015.

- [11] Mapping and modelling cadastral boundaries using drones and photogrammetry software. <https://3dsurvey.si/case-studies/mapping-and-modelling-cadastral-boundaries-using-drones-and-photogrammetry-software>, 2016.
- [12] Drones for hazard assessment and disaster management. <https://www.akdn.org/press-release/drones-hazard-assessment-and-disaster-management>, 2019.
- [13] Here are the world's largest drone companies and manufacturers to watch. <https://www.businessinsider.com/drone-manufacturers-companies-invest-stocks>, 2020.
- [14] Drones for land clarification and the empowerment of women. Global knowledge, Cities Alliance, 2020. URL https://www.citiesalliance.org/sites/default/files/2020-09/Rapport_final_IRDAC_2020_EN_0.pdf.
- [15] Disaster risk management. <https://www.worldbank.org/en/topic/disasterriskmanagement/overview>, April 2020.
- [16] Who owns what? <https://www.economist.com/leaders/2020/09/12/who-owns-what>, September 2020.
- [17] A safer, more resilient world: Reducing disaster risks with ai. <https://www.itu.int/en/myitu/News/2020/10/20/14/54/AI-for-Good-Disaster-Risk-Reduction-artificial-intelligence>, October 2020.
- [18] Odm – a command line toolkit to generate maps, point clouds, 3d models and dems from drone, balloon or kite images. <https://github.com/OpenDroneMap/ODM>, 2020.
- [19] Opensfm: Open source structure-from-motion pipeline. <https://github.com/mapillary/OpenSfM>, 2020.

- [20] Fema preliminary damage assessment guide. <https://www.fema.gov/disaster/how-declared/preliminary-damage-assessments/guide>, 2021.
- [21] NOAA National Centers for Environmental Information (NCEI) U.S. Billion-dollar Weather and Climate Disasters. <https://www.ncdc.noaa.gov/billions/>, 2021.
- [22] Drone mapping software - OpenDroneMap. <https://www.opendronemap.org/>, 2021.
- [23] QGIS - a free and open source geographic information system. <https://qgis.org/en/site/>, 2021.
- [24] Virginia roads open data: Virginia parcels (map service). <https://www.virginiaroads.org/datasets/virginia-parcels-map-service>, 2021.
- [25] Heavy rains cause flooding and landslides in Hurley, Virginia, rescue crews in area. <https://wcyb.com/news/local/flooding-reported-in-hurley-county-supervisor-urges-people-in-area-to-stay-home>, 2021.
- [26] Weather-related disasters increase over past 50 years, causing more damage but fewer deaths. <https://public.wmo.int/en/media/press-release/weather-related-disasters-increase-over-past-50-years-causing-more-damage-fewer/>, 2021.
- [27] Flash - flooded locations and simulated hydrographs project. <https://inside.nssl.noaa.gov/flash/>, 2022.
- [28] HEC-RAS. <https://www.hec.usace.army.mil/software/hec-ras/>, 2022.
- [29] Selecting an appropriate grid size and time step. <https://www.hec.usace.army.mil/confluence/rasdocs/r2dum/latest/running-a-model-with-2d-flow-areas/selecting-an-appropriate-grid-size-and-time-step>, 2022.

- [30] Creating land cover, manning's n values, and % impervious layers. <https://www.hec.usace.army.mil/confluence/rasdocs/r2dum/latest/developing-a-terrain-model-and-geospatial-layers/creating-land-cover-mannings-n-values-and-impervious-layers>, 2022.
- [31] Variable time step capabilities. <https://www.hec.usace.army.mil/confluence/rasdocs/r2dum/latest/running-a-model-with-2d-flow-areas/variable-time-step-capabilities>, 2022.
- [32] Mavic air 2 - up your game - dji. <https://www.dji.com/mavic-air-2>, 2022.
- [33] Nssl projects: Multi-radar/multi-sensor system (mrms). <https://www.nssl.noaa.gov/projects/mrms/>, 2022.
- [34] NOAA nssl: Mrms. https://www.nssl.noaa.gov/news/factsheets/MRMS_2015_March.16.pdf, 2022.
- [35] Operational product viewer. https://mrms.nssl.noaa.gov/qvs/product_viewer/, 2022.
- [36] Multi-sensor qpe - warning decision training division (wdtd) - virtual lab. <https://vlab.noaa.gov/web/wdtd/-/multi-sensor-qpe-1?selectedFolder=9234881>, 2022.
- [37] Qpe - radar only - warning decision training division (wdtd) - virtual lab. <https://vlab.noaa.gov/web/wdtd/-/qpe-radar-only?selectedFolder=9234881>, 2022.
- [38] Maximum streamflow - warning decision training division (wdtd) - virtual lab. <https://vlab.noaa.gov/web/wdtd/-/maximum-streamflow?selectedFolder=2190208>, 2022.

- [39] Virginia lidar downloads - overview. <https://www.arcgis.com/home/item.html?id=1e964be36b454a12a69a3ad0bc1473ce>, 2022.
- [40] Catastrophic flooding in yellowstone. <https://earthobservatory.nasa.gov/images/150010/catastrophic-flooding-in-yellowstone>, 2022.
- [41] Montana city faces painful reality following historic yellowstone flooding. <https://www.accuweather.com/en/business/montana-city-faces-painful-reality-following-historic-yellowstone-flooding/1206348>, 2022.
- [42] Usgs media alert: Usgs crews continue to measure and assess yellowstone river flood conditions and probabilities. <https://www.usgs.gov/news/state-news-release/usgs-media-alert-usgs-crews-continue-measure-and-assess-yellowstone-river>, 2022.
- [43] Basic information about surface coal mining in appalachia. <https://www.epa.gov/sc-mining/basic-information-about-surface-coal-mining-appalachia>, 2024.
- [44] Kyfromabove - kentucky's elevation data & aerial photography program. <https://kyfromabove.ky.gov/>, 2024.
- [45] Openmvs: open multi-view stereo reconstruction library. <https://github.com/cdcseacave/openMVS>, 2024.
- [46] S. Albawi, T. A. Mohammed, and S. Al-Zawi. Understanding of a convolutional neural network. In *2017 International Conference on Engineering and Technology (ICET)*, pages 1–6, 2017. doi: 10.1109/ICEngTechnol.2017.8308186.
- [47] Behnam Atazadeh, Abbas Rajabifard, Yibo Zhang, and Maryam Barzegar. Querying 3d cadastral information from bim models. *ISPRS International Journal of Geo-Information*, 8(8), 2019. doi: <https://doi.org/10.3390/ijgi8080329>.

- [48] D. Backes, G. Schumann, F.N. Teferle, and J. Boehm. Towards a high-resolution drone-based 3d mapping dataset to optimise flood hazard modelling. *ISPRS - International Archives of the Photogrammetry, Remote Sensing and Spatial Information Sciences*, XLII-2/W13:181–187, 06 2019. doi: 10.5194/isprs-archives-XLII-2-W13-181-2019.
- [49] Jose Ramon Martinez Batlle. Digital photogrammetry of historical aerial photographs using open-source software. *EarthArXiv*, 2018. doi: <https://doi.org/10.31223/osf.io/bna95>.
- [50] USACE Hydrologic Engineering Center. Creating land cover, manning’s n values, and % impervious layers. <https://www.hec.usace.army.mil/confluence/rasdocs/r2dum/6.6/developing-a-terrain-model-and-geospatial-layers/creating-land-cover-mannings-n-values-and-impervious-layers>.
- [51] Liang-Chieh Chen, Yukun Zhu, George Papandreou, Florian Schroff, and Hartwig Adam. Encoder-decoder with atrous separable convolution for semantic image segmentation. In *ECCV*, 2018.
- [52] Shih-Hong Chio and Cheng-Chu Chiang. Feasibility study using uav aerial photogrammetry for a boundary verification survey of a digitalized cadastral area in an urban city of taiwan. *Remote Sensing*, 12(10), 2020. doi: 10.3390/rs12101682.
- [53] Tashnim Chowdhury, Robin Murphy, and Maryam Rahnemoonfar. Rescuenet: A high resolution uav semantic segmentation benchmark dataset for natural disaster damage assessment, 2022. URL <https://arxiv.org/abs/2202.12361>.
- [54] PDAL Contributors. Pdal point data abstraction library, 2024. URL <https://doi.org/10.5281/zenodo.10884408>.
- [55] Marius Cordts, Mohamed Omran, Sebastian Ramos, Timo Rehfeld, Markus Enzweiler,

- Rodrigo Benenson, Uwe Franke, Stefan Roth, and Bernt Schiele. The cityscapes dataset for semantic urban scene understanding. In *Proc. of the IEEE Conference on Computer Vision and Pattern Recognition (CVPR)*, 2016.
- [56] P. Costabile, C. Costanzo, D. Ferraro, F. Macchione, and G. Petaccia. Performances of the new hec-ras version 5 for 2-d hydrodynamic-based rainfall-runoff simulations at basin scale: Comparison with a state-of-the art model. *Water*, 12(9), 2020. ISSN 2073-4441. doi: 10.3390/w12092326. URL <https://www.mdpi.com/2073-4441/12/9/2326>.
- [57] S. Daftry, C. Hoppe, and H. Bischof. Building with drones: Accurate 3d facade reconstruction using mavs. In *2015 IEEE International Conference on Robotics and Automation (ICRA)*, pages 3487–3494, 2015. doi: 10.1109/ICRA.2015.7139681.
- [58] Ben Dickson. What are convolutional neural networks (cnn)? <https://bdtechtalks.com/2020/01/06/convolutional-neural-networks-cnn-convnets/>, January 2020.
- [59] DJI. Consumer drones comparison. <https://www.dji.com/products/comparison-consumer-drones>.
- [60] DrivenData. Open cities ai challenge: Segmenting buildings for disaster resilience. <https://github.com/drivendataorg/open-cities-ai-challenge/>, 2020.
- [61] U.S. EPA. The effects of mountaintop mines and valley fills on aquatic ecosystems of the central appalachian coalfields (2011 final). Technical report, U.S. Environmental Protection Agency, Washington, DC, EPA/600/R-09/138F, 2011.
- [62] FEMA. Hazus. <https://www.fema.gov/flood-maps/products-tools/hazus>, 2021.
- [63] FEMA. Fema flood map service center: Hazus. <https://msc.fema.gov/portal/resources/hazus>, 2022.

- [64] Food and Agriculture Organization of the United Nations. Soil and water assessment tool (swat). <https://www.fao.org/land-water/land/land-governance/land-resources-planning-toolbox/category/details/en/c/1111246/>.
- [65] GDAL/OGR contributors. *GDAL/OGR Geospatial Data Abstraction software Library*. Open Source Geospatial Foundation, 2024. URL <https://gdal.org>.
- [66] S. Ghaffarian and N. Kerle. Towards post-disaster debris identification for precise damage and recovery assessments from uav and satellite images. *The International Archives of the Photogrammetry, Remote Sensing and Spatial Information Sciences*, XLII-2/W13:297–302, 2019. doi: 10.5194/isprs-archives-XLII-2-W13-297-2019. URL <https://www.int-arch-photogramm-remote-sens-spatial-inf-sci.net/XLII-2-W13/297/2019/>.
- [67] William C. Haneberg. Precipitation patterns, mountaintop removal mining, and the july 2022 north fork kentucky river flood. *Environmental & Engineering Geoscience*, 30(3):131–145, 08 2024. ISSN 1078-7275. doi: 10.21663/EEG-D-24-00011. URL <https://doi.org/10.21663/EEG-D-24-00011>.
- [68] Chelsea Harvey and E&E News. Three reasons appalachia’s risk of deadly floods keeps rising. <https://www.scientificamerican.com/article/three-reasons-appalachias-risk-of-deadly-floods-keeps-rising>, 2022.
- [69] C.H. Homer, J.A. Fry, and C.A. Barnes. The national land cover database, u.s. geological survey fact sheet 2012-3020. <https://pubs.usgs.gov/fs/2012/3020/fs2012-3020.pdf>, 2012.
- [70] Dustin Jones. At least 25 people have died in kentucky’s devastating floods, governor says. <https://www.npr.org/2022/07/30/1114706847/kentucky-flood-deaths>, 2022.

- [71] Diana Kaneva. Let's face facts, these mountains won't grow back: Reducing the environmental impact of mountaintop removal coal mining in appalachia. *Wm. & Mary Envtl L. & Pol'y Rev.* 931, X35, 05 2011. URL <https://scholarship.law.wm.edu/wmelpr/vol35/iss3/5/>.
- [72] Julian Keil, Dennis Edler, Thomas Schmitt, and Frank Dickmann. Creating immersive virtual environments based on open geospatial data and game engines. *KN - Journal of Cartography and Geographic Information*, 71:53–65, 2021. doi: <https://doi.org/10.1007/s42489-020-00069-6>.
- [73] M Kucharczyk and C.H. Hugenholtz. Remote sensing of natural hazard-related disasters with small drones: Global trends, biases, and research opportunities. *Remote Sensing of Environment*, 264:112577, 2021. ISSN 0034-4257. doi: <https://doi.org/10.1016/j.rse.2021.112577>. URL <https://www.sciencedirect.com/science/article/pii/S0034425721002972>.
- [74] M. Lee and K. Grosfield. More than 20 buchanan county homes destroyed, dozens evacuated as community braces for more rain. <https://www.wjhl.com/news/local/more-than-20-buchanan-county-homes-destroyed-dozens-evacuated-as-community-braces-for-more-rain/>, 2021.
- [75] M. Lee and B. Marais. Flooded hurley community faces long road to recovery as disaster relief continues. <https://www.wjhl.com/news/local/flooded-hurley-community-faces-long-road-to-recovery-as-disaster-relief-continues/>, 2021.
- [76] Tsung-Yi Lin, Priya Goyal, Ross Girshick, Kaiming He, and Piotr Dollár. Focal loss for dense object detection. In *2017 IEEE International Conference on Computer Vision (ICCV)*, pages 2999–3007, 2017. doi: 10.1109/ICCV.2017.324.

- [77] Ilya Loshchilov and Frank Hutter. Decoupled weight decay regularization, 2017. URL <https://arxiv.org/abs/1711.05101>.
- [78] Lauren Masey. Disaster risk reduction: How big data plays a role in its ambiguity. <http://sites.utexas.edu/climatesecurity/2020/03/01/big-data-and-what-it-means-for-action/>, March 2020.
- [79] John McCracken. How coal mining increased east kentucky’s flood risk. <https://grist.org/energy/how-coal-mining-increased-east-kentuckys-flood-risk/>, 2022.
- [80] S.M.S. Mohd Daud, M.Y.P. Mohd Yusof, C.C. Heo, L.S. Khoo, M.K. Chainchel Singh, M.S. Mahmood, and H Nawawi. Applications of drone in disaster management: A scoping review. *Science & Justice*, 62(1):30–42, 2022. ISSN 1355-0306. doi: <https://doi.org/10.1016/j.scijus.2021.11.002>. URL <https://www.sciencedirect.com/science/article/pii/S1355030621001477>.
- [81] Giuseppe Molinaro and Vivien Deparday. Demystifying machine learning for disaster risk management. <https://blogs.worldbank.org/opendata/demystifying-machine-learning-disaster-risk-management>, March 2019.
- [82] M. Moore and M. Lee. Fema denies individual assistance for hurley residences ravaged by floods. <https://www.wjhl.com/news/local/fema-denies-individual-assistance-for-hurley-residences-ravaged-by-floods/>, 2021.
- [83] J. Myers. Which natural disasters hit most frequently? <https://www.weforum.org/agenda/2016/01/which-natural-disasters-hit-most-frequently>, 2016.
- [84] T. Myers. Multiple disasters strain response systems, slow recovery, and deepen

- inequity. <https://www.directrelief.org/2020/10/multiple-disasters-strain-response-slow-recovery-and-worsen-injustice/>, 2020.
- [85] Liam Niemeyer. Surface coal mining worsened deadly eastern kentucky floods in july 2022, study shows. <https://kentuckylantern.com/2024/07/22/surface-coal-mining-worsened-deadly-eastern-kentucky-floods-in-july-2022-study-shows/>, 2024.
- [86] Michael Osborne. Mission planner. <https://github.com/ArduPilot/MissionPlanner>.
- [87] United Nations OCHA. 5 essentials for the first 72 hours of disaster response. <https://medium.com/humanitarian-dispatches/5-essentials-for-the-first-72-hours-of-disaster-response-51746452bc88>, 2017.
- [88] N. Ongdas, F. Akiyanova, Y. Karakulov, A. Muratbayeva, and N. Zinabdin. Application of hec-ras (2d) for flood hazard maps generation for yesil (ishim) river in kazakhstan. *Water*, 12(10), 2020. ISSN 2073-4441. doi: 10.3390/w12102672. URL <https://www.mdpi.com/2073-4441/12/10/2672>.
- [89] Yue Pan, Yiqing Dong, Dalei Wang, Airong Chen, and Zhen Ye. Three-dimensional reconstruction of structural surface model of heritage bridges using uav-based photogrammetric point clouds. *Remote Sensing*, 11(1204), 2019. doi: <https://doi.org/10.3390/rs11101204>.
- [90] Yalong Pi, Nipun Nath, and Amir Behzadan. Detection and semantic segmentation of disaster damage in uav footage. *Journal of Computing in Civil Engineering*, 35: 04020063, 03 2021. doi: 10.1061/(ASCE)CP.1943-5487.0000947.

- [91] PreventionWeb. Datasets - understanding disaster risk data. <https://www.preventionweb.net/risk/datasets>, November 2015.
- [92] A. Restas. Drone applications for supporting disaster management. *World Journal of Engineering and Technology*, 3:316–321, 2015. doi: 10.4236/wjet.2015.33C047.
- [93] Olaf Ronneberger, Philipp Fischer, and Thomas Brox. U-net: Convolutional networks for biomedical image segmentation. *CoRR*, abs/1505.04597, 2015. URL <http://arxiv.org/abs/1505.04597>.
- [94] Adrian Rosebrock. Intersection over union (iou) for object detection. <https://pyimagesearch.com/2016/11/07/intersection-over-union-iou-for-object-detection/>, 2016.
- [95] Sumit Saha. A comprehensive guide to convolutional neural networks — the eli5 way. <https://towardsdatascience.com/a-comprehensive-guide-to-convolutional-neural-networks-the-eli5-way-3bd2b1164a53>, December 2018.
- [96] Brendan Schulman. Why did dji create a 249-gram drone? <https://content.dji.com/why-did-dji-create-a-249-gram-drone/>, October 2019.
- [97] Evan Shelhamer, Jonathan Long, and Trevor Darrell. Fully convolutional networks for semantic segmentation. *CoRR*, abs/1605.06211, 2016. URL <http://arxiv.org/abs/1605.06211>.
- [98] Maciej Smaczyński and Tymoteusz Horbiński. Creating a 3d model of the existing historical topographic object based on low-level aerial imagery. *KN - Journal of Cartography and Geographic Information*, 71:33–43, 2021. doi: <https://doi.org/10.1007/s42489-020-00061-0>.

- [99] United States Department of Agriculture Soil Survey Staff, Natural Resources Conservation Service. Web soil survey. <https://websoilsurvey.nrcs.usda.gov/app/>.
- [100] sUASNews. Pix4d mapping nepal: Drones and the future of disaster response. <https://www.suasnews.com/2015/11/pix4d-mapping-nepal-drones-and-the-future-of-disaster-response/>, November 2015.
- [101] SWAT. Global data - swat us ssurgo soils database. <https://swat.tamu.edu/data/>, 2022.
- [102] S. Teague. Update: 1 killed in buchanan county floods. <https://www.wjhl.com/news/local/update-1-killed-in-buchanan-county-floods/>, 2021.
- [103] USGS. North fork kentucky river at jackson, ky - usgs water data for the nation. <https://waterdata.usgs.gov/monitoring-location/03280000>.
- [104] Anand Vetrivel, Markus Gerke, Norman Kerle, and George Vosselman. Identification of structurally damaged areas in airborne oblique images using a visual-bag-of-words approach. *Remote Sensing*, 8(3), 2016. ISSN 2072-4292. doi: 10.3390/rs8030231. URL <https://www.mdpi.com/2072-4292/8/3/231>.
- [105] J. Wang, Y. Hong, L. Li, J.J. Gourley, S.I. Khan, K.K. Yilmaz, R.F. Adler, F.S. Policelli, S. Habib, D. Irwn, A.S. Limaye, T. Korme, and L. Okello. The coupled routing and excess storage (crest) distributed hydrological model. *Hydrological Sciences Journal*, 56(1):84–98, 2011. doi: 10.1080/02626667.2010.543087. URL <https://doi.org/10.1080/02626667.2010.543087>.
- [106] Daniel Whitehurst, Brianna Friedman, Kevin Kochersberger, Venkat Sridhar, and James Weeks. Drone-based community assessment, planning, and disaster risk management for sustainable developmen. *Remote Sensing*, 13, 2021. doi: 10.3390/rs13091739.

- [107] Daniel Whitehurst, Kunal Joshi, Kevin Kochersberger, and James Weeks. Post-flood analysis for damage and restoration assessment using drone imagery. *Remote Sensing*, 14, 2022. doi: 10.3390/rs14194952.
- [108] L. Wouters, A. Couasnon, M. C. de Ruiter, M. J. C. van den Homberg, A. Teklesadik, and H. de Moel. Improving flood damage assessments in data-scarce areas by retrieval of building characteristics through uav image segmentation and machine learning – a case study of the 2019 floods in southern malawi. *Natural Hazards and Earth System Sciences*, 21(10):3199–3218, 2021. doi: 10.5194/nhess-21-3199-2021. URL <https://nhess.copernicus.org/articles/21/3199/2021/>.
- [109] L. Wouters, A. Couasnon, M. C. de Ruiter, M. J. C. van den Homberg, A. Teklesadik, and H. de Moel. Improving flood damage assessments in data-scarce areas by retrieval of building characteristics through uav image segmentation and machine learning – a case study of the 2019 floods in southern malawi. *Natural Hazards and Earth System Sciences*, 21(10):3199–3218, 2021. doi: 10.5194/nhess-21-3199-2021. URL <https://nhess.copernicus.org/articles/21/3199/2021/>.
- [110] Lang Xia, Ruirui Zhang, Liping Chen, Longlong Li, Tongchuan Yi, Yao Wen, Chenchen Ding, and Chunchun Xie. Evaluation of deep learning segmentation models for detection of pine wilt disease in unmanned aerial vehicle images. *Remote Sensing*, 13(18), 2021. ISSN 2072-4292. doi: 10.3390/rs13183594. URL <https://www.mdpi.com/2072-4292/13/18/3594>.
- [111] Enes Yildirim, Craig Just, and Ibrahim Demir. Flood risk assessment and quantification at the community and property level in the state of iowa. *International Journal of Disaster Risk Reduction*, 77:103106, 2022. ISSN 2212-4209. doi: <https://doi.org/10.1016/j.ijdrr.2022.103106>.

- [112] Hengshuang Zhao, Jianping Shi, Xiaojuan Qi, Xiaogang Wang, and Jiaya Jia. Pyramid scene parsing network. *CoRR*, abs/1612.01105, 2016. URL <http://arxiv.org/abs/1612.01105>.
- [113] Xiaoyu Zhu, Junwei Liang, and Alexander Hauptmann. Msnet: A multilevel instance segmentation network for natural disaster damage assessment in aerial videos, 2020. URL <https://arxiv.org/abs/2006.16479>.
- [114] Tomasz Zwęgliński. The use of drones in disaster aerial needs reconnaissance and damage assessment – three-dimensional modeling and orthophoto map study. *Sustainability*, 12(15), 2020. ISSN 2071-1050. doi: 10.3390/su12156080. URL <https://www.mdpi.com/2071-1050/12/15/6080>.